Hindawi
Computational and Mathematical Methods
Volume 2023, Article ID 6671523, 20 pages
https://doi.org/10.1155/2023/6671523

Research Article

Dual Solutions and Stability Analysis of Cu-H_2O-Casson Nanofluid Convection past a Heated Stretching/Shrinking Slippery Sheet in a Porous Medium

Kifle Adula Duguma,[1] **Oluwole Daniel Makinde**,[2] **and Lemi Guta Enyadene**[1]

[1]*Department of Applied Mathematics, Adama Science and Technology University, Oromia, Ethiopia*
[2]*Faculty of Military Science, Stellenbosch University, South Africa*

Correspondence should be addressed to Kifle Adula Duguma; kifle.adula@astu.edu.et

Received 8 December 2022; Revised 16 January 2023; Accepted 6 May 2023; Published 18 May 2023

Academic Editor: Akbar Ali

In this study, we examined the impact of Cu-H_2O nanoparticles on two-dimensional Casson nanofluid flows past permeable stretching/shrinking sheet embedded in a Darcy-Forchheimer porous medium in the presence of slipperiness of surface, suction/injection, viscous dissipation, and convective heating. Using some realistic assumptions and appropriate similarity transformations, the governing nonlinear partial differential equations were formulated and transformed into a system of nonlinear ordinary differential equations and then numerically solved by using the shooting technique. Numerical results are displayed for dimensionless fluid velocity and temperature profiles, skin friction, and the local Nusselt number. The impacts of different governing physical parameters on these quantities are presented and discussed using graphs, tables, and a chart. For the specific range of shrinking sheet, the result shows that dual solutions exist, and temporal stability analysis is performed by introducing small disturbances to determine the stable solutions. It is detected that the upper branch solution is hydrodynamically stable and substantially realistic; however, the lower branch solution is unstable and physically unachievable. The fluid flow stability is obtained by enhancing the suction, surface slipperiness, and viscous dissipation parameters. However, augmenting the values of the Casson factor, Cu-H_2O nanoparticle volume fraction, porous medium, porous medium inertia, and convective heating parameters increases the blow-up stability of the fluid flow. The rate of heat transfer enhances with the increment in the Casson factor, porous medium, porous medium inertia, suction, velocity ratio, nanoparticle volume fraction, and convective heating parameters, whereas it reduces as the slipperiness of the surface and viscous dissipation parameters rise. Increment of Cu-H_2O nanoparticle volume fraction into the Casson fluid boosts the heat transfer enhancement rate higher for the shrinking sheet surface.

1. Introduction

For a few decades, researchers have given due attention to the study of non-Newtonian fluids due to their significant features in the fields of industrial processes and technological sciences, such as polymer engineering, certain separation processes, manufacturing of papers and foods, and petroleum drilling, according to Bhattacharyya [1]. For instance, drilling muds, synthetic lubricants, clay coating, biological fluids like blood, certain oils, paints, and sugar solutions are common cases of non-Newtonian fluid types. The fundamental equations of Navier-Stokes cannot momentarily define the characteristics of the non-Newtonian fluid flow field due to the complexity in the mathematical expression of the flow problem. For non-Newtonian fluid, several models are defined based on rheological qualities, such as Bulky, Casson, Eyring-Powell, Seely, Oldroyd-B, Maxwell, Oldroyd-A, Carreau, Jeffrey, and Burger. From these models, the Casson model [2] is the most important model for the suspension and blood properties in our daily life.

Magnetohydrodynamic Casson fluid under the aligned magnetic field with inconstant thickness was investigated by Saravana et al. [3]. Zhang et al. [4] studied the heat transport characteristic flow of the Casson fluid with electroosmosis forces. Recently, heat transfer on the Casson nanofluid overflow past a Riga plate (one of the external agents used to limit the friction force and control the flow of fluid) was investigated by Upreti et al. [5].

For its frequent applications in industrial and engineering, the theme of flow nanofluids has attracted due attention. Tawari and Das [6] did an analysis on nanofluids. Gupta et al. [7] discovered the astonishing thermal properties of nanofluids and improved the causes of nanofluids' thermal conductivity. In many industrial processes, heating and cooling of fluids are fundamental demands such as power manufacturing and delivery. Frequently, there is a need to enhance the process of cooling of high-energy equipment. [8–10] worked on how to improve the thermal conductivity of fluids, so that the heat transfer of the fluid enhances. Eastman et al. [11] investigated enhancements in thermal conductivity of fluid using Cu nanofluids, where just a 0.3% volume fraction of 10 nm diameter Cu nanoparticles led to an increment of up to 40% in the ethylene glycol thermal conductivity. Moreover, the convection heat transfer of nanofluids was also investigated by different researchers, and based on that, significant improvement was reported in the heat transfer rate. Zubair et al. [12] did an analysis on the magnetohydrodynamic Casson nanofluid flow with entropy generation in the presence of viscous dissipation. Saeed et al. [13] demonstrated three-dimensional Casson's nanofluid flow past a rotating inclined disk with the influence of heat absorption/production. Khan et al. [14] studied the impact of an induced magnetic field on mixed convective stagnation flow of TiO_2-Cu-H_2O hybrid nanofluid towards a stretchable sheet surface. Rizwana et al. [15] concentrated on the non-Newtonian fluid flow at an oblique stagnation point of Cu-H_2O nanofluid flow, concluding that the Casson fluid parameter makes the fluid velocity faster and decreases the boundary layer while the temperature profile drops with non-Newtonian parameter β and nanoparticle volume fraction ϕ, and the system heats up by the impact of viscous dissipation. More discussion on heat transfer enhancement is detailed by Lund et al. [16] and Hussanan et al. [17].

Due to its enormous applications in areas of industry and engineering, according to Hayat et al. [18], the boundary layer flows of non-Newtonian fluids and the heat transfer properties due to a stretching sheet surface have attracted researchers' attention. Crane [19] investigated the viscous fluid flows because of linearly stretching surface problems. Tamoor et al. [20] studied the MHD flow of Casson's fluid past a stretching cylinder. In contrast to stretching sheets, Wang [21] considered shrinking sheets, which exhibit quite different properties from that of the stretching sheet flow. In the shrinking surface case, because of the free-range fluid flow happening in the boundary layer, no possible solution is obtained. Consequently, the addition of a sufficient amount of wall mass suction (which controls the vorticity produced because of the shrinking of the sheet within the boundary layer) by Miklavcic and Wang [22] or by adding stagnation flow by Wang [23] may guarantee the existence of a solution that is not unique. This leads to the existence of a nonunique solution for the system of governing differential equations. For the non-unique solutions obtained, we use a mathematical technique (called temporal stability analysis) that is used for testing temporal stability. Experimentally, the lower branch solution which is a part of the solution of the system differential equations cannot be produced and, hence, should be analyzed. Nazar et al. [24] examined a nanofluid stagnation-point flow over a shrinking sheet. Layek et al. [25] presented boundary layer stagnation-point flow of non-Newtonian fluids past a shrinking/stretching sheet and showed that as the value of the velocity ratio (shrinking/stretching) parameter increases, the velocity and thermal boundary layer thicknesses decrease. Again, Mandal and Layek [26] investigated the unsteady magnetohydrodynamic (MHD) mixed convective Casson fluid flow over a flat surface in the presence of slip conditions and blowing/suction and obtained significant results. More flow stability analysis and testing for the existence of a dual solution were detailed in the literature [27–30].

Studies of fluid flow and heat transfer in a porous medium have attracted the attention of researchers towards fluid flow in porous media for the past several decades because of the wide range of applications, such as water developments in geothermal supplies and drying technologies. For simulating porous media there are the Darcy, non-Darcy, and nonequilibrium models. For low-velocity flow with weak porosity conditions, a pioneering semi-empirical equation was developed by Darcy. Accordingly, Forchheimer [31] prophesied a modified equation known as the Darcy-Forchheimer equation by introducing quadratic terms in the governing momentum equation of the fluid flow. Harris et al. [32] studied mixed convection boundary-layer flow over a vertical surface through a porous medium using the Brinkman model with slip. The Brinkman-extended Darcy model was used by Dogonchi et al. [33] to explore the natural convection of a Cu-H_2O nanofluid across a porous medium and obtain the Darcy number which has a direct relationship with the intensity of the convective flow across the medium. Shaw et al. [34] studied the application to brain dynamics of the impact of entropy generation on the Darcy-Forchheimer flow of $MnFe_2O_4$-Casson/water nanofluid because of a rotating disk. In their recent study, Upreti et al. [35] discussed the hydromagnetic stagnation point magnetite ferrofluid flow over a convectively heated shrinking/stretching permeable sheet surface which is exposed to injection/suction in a Darcy-Forchheimer porous medium. Joshi et al. [36] investigated the Darcy-Forchheimer flow model in a three-dimensional case and the heat transfer phenomenon of H_2O-CNT nanofluid on a two-way stretchable surface, and it was observed that with an enhancement in the Eckert numbers along the two directions, for temperature curves, two patterns were obtained, the initial temperature outlines rose, and after that, they diminished. Moreover, Tadesse et al. [37] studied the overall influence of blowing/suction

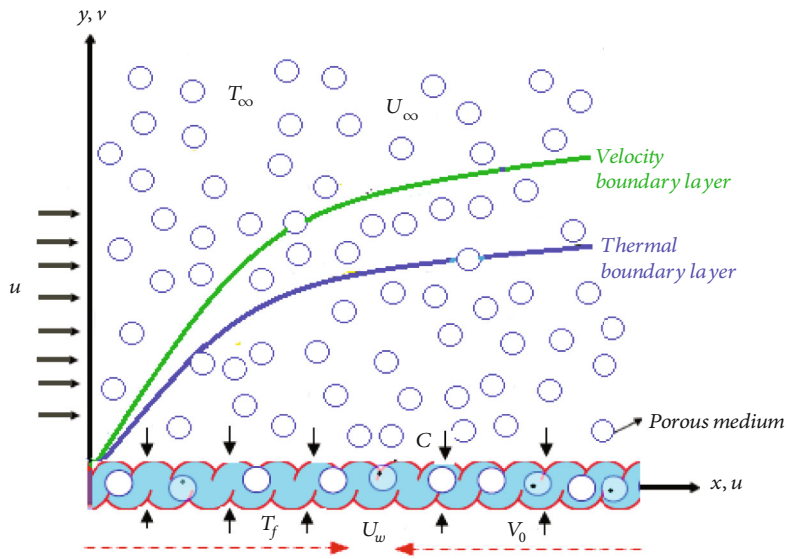

Figure 1: Physical model of flow.

on the MHD flow of Cu-Ag/H_2O-$C_2H_6O_2$ hybrid nanofluid through a stretchable surface in Darcy-Forchheimer porous medium and found that velocity drops in the case of suction and absence of suction/injection region, on augmenting the values of Forchhiemer, and porosity parameters, and for blowing region, dual behavior is observed in velocity profiles with a rise in Forchhiemer and porosity parameters.

A thorough observation of the aforementioned above-cited reviews and works reveals that no scientific analysis has been done to study the mutual effects of the slipperiness of the surface, nanoparticle volume fraction, thermal and viscous dissipation, porous media, and stretching/shrinking surface on the rate of heat transfer enhancement in a flow into the boundary layer of the Cu-H_2O-Casson nanofluids. Filling the gap in the work of Upreti et al. [35] (in which they consider MHD Newtonian flow), this paper considers non-Newtonian flow subjected to a slippery surface. Since in this type of fluid flow problem, dual solutions possibly exist due to stretching/shrinking surface, the main goal of this paper is to do stability analysis to determine physically reliable and stable solutions and enhancement of heat transfer as a result of adding the Cu-H_2O nanoparticle to non-Newtonian Casson fluids for the coupled transformed ordinary differential equations. Moreover, the numerical results of the coefficient of skin friction, rates of heat transfer, and velocity and temperature profiles are demonstrated and discussed both graphically and quantitatively. Thermally driven boundary layer flow of the Casson nanofluid in a porous medium has several applications in chemical and mechanical engineering, e.g., food processing and storage, geophysical systems, electrochemistry, fibrous insulation, metallurgy, the design of pebble bed nuclear reactors, underground disposal of nuclear or nonnuclear waste, and microelectronics cooling. Casson's nanofluid is more helpful for cooling and friction-reducing agents compared to Newtonian-type nanofluid flow.

2. Mathematical Description of the Problem

Consider the two-dimensional, viscous, homogeneous, steady, isotropic, laminar, and incompressible boundary layer flow of a Cu-H_2O-Casson nanofluid over a linearly stretching/shrinking sheet within a Darcy-Forchheimer porous medium. The flow is subjected to suction/injection of constant velocity V_0 perpendicular to the sheet surface. The shrinking/stretching sheet moves with velocity $U_w = ax$, and the flow is subjected to slip condition. The surface below the shrinking/stretching sheet surface is heated convectively by a hot fluid having an initial temperature T_f that gives a heat transfer coefficient h_f, and the ambient temperature of the Casson nanofluid is taken as T_∞. Geometrical orientation for the flow considers the Cartesian coordinate system where the x-axis is taken as the shrinking/stretching sheet surface, and the y-axis is perpendicular to the sheet surface so that the flow is confined to the half plane $y > 0$, as the physical model shown in Figure 1.

The rheological equation of an isotropic and incompressible flow of a Casson fluid can be written based on Nakamura and Sawada [38] and Animasaun [39] as

$$\tau_{ij} = \begin{cases} 2\left(\mu_B + \dfrac{p_y}{\sqrt{2\pi}}\right)e_{ij} & \text{if } \pi > \pi_c \\ 2\left(\mu_B + \dfrac{p_y}{\sqrt{2\pi_c}}\right)e_{ij} & \text{if } \pi < \pi_c \end{cases}, \quad (1)$$

where τ_{ij} represents components of the stress tensor, μ_B is the plastic dynamic viscosity of the non-Newtonian fluid, $p_y \equiv \mu_B\sqrt{2\pi_c}/\beta$ is the yield stress of the fluid, β is the non-

Newtonian Casson parameter, $\pi = e_{ij}e_{ij}$ is the $(i,j)^{th}$ deformation rate component (product of the rate of strain tensor with itself), $e_{ij} = 1/2[(\partial u_i/\partial x_j)/(\partial u_j/\partial x_i)]$ is the rate of strain tensor, and π_c is a critical value of π, which is based on the non-Newtonian model. Some non-Newtonian fluids (for instance rheopectic fluids) require a gradually enhancing shear stress to get a constant strain rate. For the Casson fluid flow under consideration, $\pi > \pi_c$, and the dynamic viscosity is defined as $\mu_f = \mu_B + p_y/\sqrt{2\pi}$, and hence, the kinematic viscosity becomes

$$\nu_f = \frac{\mu_B}{\rho_f}\left(1 + \frac{1}{\beta}\right). \tag{2}$$

Adopting the Darcy-Forchheimer flow model, Tiwari-Das [6] convective transport model equations, for this investigation, the governing equations are formulated from the balance of continuity, linear momentum, and energy past a permeable shrinking/stretching sheet surface, with respect to a Cartesian coordinate; x-y system is given by Tshivhi and Makinde [28] and Tadesse et al. [37] as

$$\frac{\partial u}{\partial x} + \frac{\partial v}{\partial y} = 0, \tag{3}$$

$$u\frac{\partial u}{\partial x} + v\frac{\partial u}{\partial y} = U_\infty \frac{dU_\infty}{dx} + \frac{\mu_{nf}}{\rho_{nf}}\left(1 + \frac{1}{\beta}\right)\frac{\partial^2 u}{\partial y^2} - \frac{\mu_{nf}}{\rho_{nf}k_1}\left(1 + \frac{1}{\beta}\right)\cdot (u - U_\infty) - \frac{F}{\rho_{nf}\sqrt{k_1}}(u - U_\infty)^2, \tag{4}$$

$$u\frac{\partial T}{\partial x} + v\frac{\partial T}{\partial y} = \frac{k_{nf}}{(\rho C_p)_{nf}}\frac{\partial^2 T}{\partial y^2} + \frac{\mu_{nf}}{(\rho C_p)_{nf}}\left(1 + \frac{1}{\beta}\right)\left(\frac{\partial u}{\partial y}\right)^2 + \frac{\mu_{nf}}{(\rho C_p)_{nf}k_1}\left(1 + \frac{1}{\beta}\right)(u - U_\infty)^2 + \frac{F}{(\rho C_p)_{nf}\sqrt{k_1}}(u - U_\infty)^3, \tag{5}$$

with the subjected boundary conditions given by

$$u(x,0) = U_w(x) + \frac{\mu_f}{L}\left(1 + \frac{1}{\beta}\right)\frac{\partial u}{\partial y},\ v(x,0) = V_0,$$
$$-k_f\frac{\partial T}{\partial y}(x,0) = h_f\left[T_f(x) - T(x,0)\right],\ u(x,\infty) \longrightarrow U_\infty(x),\ T(x,\infty) \longrightarrow T_\infty, \tag{6}$$

where u is the x component and v is the y component of the Casson nanofluid velocity. $U_\infty = bx$ is the free stream velocity of the Casson fluid, α is the thermal diffusivity of the fluid, μ_{nf} is the effective dynamic viscosity of the Casson nanofluid, β is the non-Newtonian or Casson parameter, ρ_{nf} is the effective density of the Casson nanofluid, k_{nf} is the effective thermal conductivity of the nanofluid, k_1 is the permeability of the porous medium, F is the Forchheimer drag force coefficient, T is the temperature of the fluid, $(\rho C_p)_{nf}$ is the effective heat capacity of the Casson nanofluid, C_p is the specific heat at a constant pressure of the fluid, μ_f is the dynamic viscosity of the fluid, L is the slip length coefficient, k_f is the thermal conductivity of the fluid, h_f is the convective heat transfer coefficient, $T_f = T_\infty + nx^2$ is the convective fluid temperature below the stretching/shrinking sheet, a is the constant of the linear stretching rate (s^{-1}) of the Casson fluid, and b is the constant of the linear stretching/shrinking rate (s^{-1}) of the wall (stretching for $b > 0$ and shrinking for $b < 0$). The parameters μ_{nf}, ρ_{nf}, k_{nf}, and $(\rho C_p)_{nf}$ are defined by Tadesse et al. [37] as

$$\begin{aligned}
\mu_{nf} &= \mu_f(1-\phi)^{-2.5},\\
k_{nf} &= \frac{k_s + 2k_f - 2\phi(k_f - k_s)}{k_s + 2k_f + \phi(k_f - k_s)}k_f,\\
\rho_{nf} &= (1-\phi)\rho_f + \phi\rho_s,\\
(\rho C_p)_{nf} &= (1-\phi)(\rho C_p)_f + \phi(\rho C_p)_s,
\end{aligned} \tag{7}$$

where ρ_f, ρ_s, k_f, k_s, ϕ and μ_f are the density of the base fluid, density of the solid nanoparticle, base fluid thermal conductivity, nanoparticle thermal conductivity, nanoparticle volume fraction, and base fluid dynamic viscosity, respectively. Note that

$$k_{nf} = \frac{k_s + (n-1)k_f - (n-1)\phi(k_f - k_s)}{k_s + (n-1)k_f + \phi(k_f - k_s)}k_f. \tag{8}$$

$n = 3/\Psi$, where Ψ, called the "sphericity," is defined as the ratio of the surface area of the sphere to that of the particle for the same volume. For spherical particles, $\Psi = 1$, and for the cylinders, $\Psi = 0.5$. This study considers the copper particle and is spherical in shape, so that $n = 3$, according to Hamilton and Crosser [40]. The thermophysical properties of nanoparticles and base fluid at $T = 300K$ are given in Table 1, according to Tshivhi and Makinde [28] and Shaw et al. [34].

The above Equations (4)–(6) represent the governing equations of the nanofluid flow when $\beta \longrightarrow \infty$ and the Casson fluid flow when $\beta \neq \infty$ and $\phi = 0$. Equations (3)–(5) can be transformed to the dimensionless form by using the non-dimensional variables below to obtain the similarity solutions by Tadesse et al. [37].

$$u = axf'(\eta),\ v = -\sqrt{a\nu_f}f(\eta),\ \eta = \sqrt{\frac{a}{\nu_f}}y,\ \theta(\eta) = \frac{T - T_\infty}{T_f - T_\infty}, \tag{9}$$

where the stream function $\psi = x\sqrt{a\nu_f}f(\eta)$ is written as a velocity component as

$$u = \frac{\partial \psi}{\partial y},\ v = -\frac{\partial \psi}{\partial x}. \tag{10}$$

Table 1: Thermophysical properties of H_2O, Casson's fluid, and Cu.

Properties	H_2O	Casson's fluid	Cu
Density, ρ (kg.m^{-3})	997.1	1060	8933
Thermal conductivity, k (W.m^{-1}.K^{-1})	0.613	0.505	401
Specific heat, C_p (J.kg^{-1}.K)	4179	3490	385

Since the continuity equation is satisfied by (9) and (10), automatically, Equations (4) and (5) are converted into the following nondimensional form:

$$\left(1+\frac{1}{\beta}\right)A_1\left[f'''-\frac{1}{Da}\left(f'-1\right)\right]+A_2\left[ff''-\left(f'\right)^2+1\right]-F_r\left(f'-1\right)^2=0\ -0.3\text{cm},\tag{11}$$

$$\frac{A_3}{\Pr}\theta''+A_4\left(f\theta'-2f'\theta\right)+A_1\,Ec\left(1+\frac{1}{\beta}\right)\times\left[\left(f''\right)^2+\frac{1}{Da}\left(f'-1\right)^2\right]+Ec\,F_r\left(f'-1\right)^3=0.\tag{12}$$

With the dimensionless form of the boundary conditions

$$f(0)=S,\ f'(0)=\lambda+\delta\left(1+\frac{1}{\beta}\right)f''(0),\ \theta'(0)=Bi[\theta(0)-1]$$
$$f'(\infty)=1,\ \theta(\infty)=0,\tag{13}$$

where η is the similarity variable, λ is the velocity ratio (stretching/shrinking) parameter where $\lambda>0$ for stretching and $\lambda<0$ for shrinking of the sheet, Da is the Darcy number (porous media parameter), F_r is the Forchheimer (second order porous resistance) parameter, Pr is the Prandtl number, Ec is the Eckert number, S is the constant mass flux parameter where $S>0$ for suction and $S<0$ for injection of the fluid, δ is the velocity slip parameter, and Bi is the Biot number (convective parameter). These dimensionless parameters and the variables A_1, A_2, A_3, and A_4 quantities are defined as

$$\begin{aligned}
\text{Da}&=\frac{\text{ak}_1}{\nu_f},\\
A_1&=(1-\phi)^{-2.5},\\
A_2&=1-\phi+\phi\frac{\rho_s}{\rho_f},\\
F_r&=\frac{xF}{\rho_f\sqrt{k_1}},\\
A_3&=\frac{k_s+2k_f-2\phi\left(k_f-k_s\right)}{k_s+2k_f+\phi\left(k_f-k_s\right)},\\
\Pr&=\frac{\nu_f\left(\rho C_p\right)_f}{k_f},\\
A_4&=1-\phi+\phi\frac{\left(\rho C_p\right)_s}{\left(\rho C_p\right)_f},\\
\text{Ec}&=\frac{U_\infty^2}{\left(C_p\right)_f\left(T_f-T_\infty\right)},\\
\delta&=\frac{\mu_f}{L}\sqrt{\frac{a}{\nu_f}},\\
S&=-\frac{V_0}{\sqrt{\text{a}\nu_f}},\\
\text{Bi}&=\frac{h_f}{k_f}\sqrt{\frac{\nu_f}{a}},\\
\lambda&=\frac{b}{a}
\end{aligned}\tag{14}$$

Note that in our discussion, F_r, Da, Pr, Ec, and Bi measure the pressure drop caused by fluid-solid interactions to that of viscous and inertia resistance ratio, the relative effect of the permeability of the porous medium versus its cross-sectional area, momentum diffusivity to thermal diffusivity ratio, kinetic energy of the flow to heat dissipation potential (enthalpy difference) ratio across the thermal boundary layer, and internal thermal resistance at the surface of the sheet to the boundary layer thermal resistance ratio, respectively.

Moreover, according to [41], the pressure gradient in the flow due to porous medium ∇P is given by

$$\nabla P=-\frac{\mu}{k_1}q-\frac{C_F\rho_f}{\sqrt{k_1}}|q|q,\tag{15}$$

where q is the velocity vector, k_1 is the permeability of the porous medium m^2, $C_F=11/20(1-11/20(d/D_e))$ is a dimensionless form-drag constant, d is the diameter of spheres of the porous medium, and $D_e=2\text{wh}/w+h$ is the equivalent diameter of the bed (defined in terms of the height h and width w of the bed). Thus, for our case, putting $F\equiv\rho C_F$ (kgm^{-3}), we obtain Fr which is dimensionless. The wall skin friction τ_w and heat flux q_w are computed as

$$\begin{aligned}
\tau_w&=\mu_{\text{nf}}\left(1+\frac{1}{\beta}\right)\left.\frac{\partial u}{\partial y}\right|_{y=0},\\
q_w&=-k_{\text{nf}}\left.\frac{\partial u}{\partial y}\right|_{y=0},
\end{aligned}\tag{16}$$

so that physical quantities of interest include the coefficient of the skin friction C_f, and the local Nusselt number Nu is given by

$$\begin{aligned} C_f &= \frac{\tau_w}{\rho_f U_w^2}, \\ Nu &= \frac{x q_w}{k_f\left(T_f - T_\infty\right)}, \\ Re_x^{1/2} C_f &= A_1\left(1 + \frac{1}{\beta}\right) f''(0), \\ Re_x^{-1/2} Nu &= -A_3\,\theta'(0), \end{aligned} \tag{17}$$

where $Re_x = xU_\infty/\nu_f$ is the local Reynold number. To compute the heat transfer enhancement (HTE) of the nanoparticles, we use the following formula:

$$\mathrm{HTE} = \frac{Nu/\sqrt{Re_x}(\phi \neq 0) - Nu/\sqrt{Re_x}(\phi = 0)}{Nu/\sqrt{Re_x}(\phi = 0)} \times 100. \tag{18}$$

Fluid flow models of such kind could have dual solutions based on the physical parameters within the problem from the numerical result obtained. Therefore, by making a stability analysis, we determine the solution which is stable and physically practicable. We perform this analysis mathematically to validate the real solution among all the others. Thus, to employ the stability analysis, Equations (4) and (5) should be rewritten in unsteady (time dependent) case, according to Merkin [42]. Thus, we have

$$\begin{aligned} \frac{\partial u}{\partial t} + u\frac{\partial u}{\partial x} + v\frac{\partial u}{\partial y} &= U_\infty \frac{dU_\infty}{\mathrm{dx}} + \frac{\mu_{\mathrm{nf}}}{\rho_{\mathrm{nf}}}\left(1 + \frac{1}{\beta}\right)\frac{\partial^2 u}{\partial y^2} \\ &\quad - \frac{\mu_{\mathrm{nf}}}{\rho_{\mathrm{nf}} k_1}\left(1 + \frac{1}{\beta}\right)(u - U_\infty) \\ &\quad - \frac{F}{\rho_{\mathrm{nf}}\sqrt{k_1}}(u - U_\infty)^2, \end{aligned} \tag{19}$$

$$\begin{aligned} \frac{\partial T}{\partial t} + u\frac{\partial T}{\partial x} + v\frac{\partial T}{\partial y} &= \frac{k_{\mathrm{nf}}}{\left(\rho C_p\right)_{\mathrm{nf}}}\frac{\partial^2 T}{\partial y^2} + \frac{\mu_{\mathrm{nf}}}{\left(\rho C_p\right)_{\mathrm{nf}}}\left(1 + \frac{1}{\beta}\right)\left(\frac{\partial u}{\partial y}\right)^2 \\ &\quad + \frac{\mu_{\mathrm{nf}}}{\left(\rho C_p\right)_{\mathrm{nf}} k_1}\left(1 + \frac{1}{\beta}\right)(u - U_\infty)^2 \\ &\quad + \frac{F}{\left(\rho C_p\right)_{\mathrm{nf}}\sqrt{k_1}}(u - U_\infty)^3, \end{aligned} \tag{20}$$

where here t is time.

Now, unsteady Equations (19) and (20) are transformed as follows:

$$\begin{aligned} u &= \mathrm{axf}'(\eta, \tau), \\ v &= -\sqrt{\mathrm{a}\nu_f} f(\eta, \tau), \\ \psi &= x\sqrt{\mathrm{a}\nu_f} f(\eta, \tau), \\ \theta(\eta, \tau) &= \frac{T - T_\infty}{T_f - T_\infty}, \\ \eta &= \sqrt{\frac{a}{\nu_f}} y, \tau = \mathrm{at}, \end{aligned} \tag{21}$$

where τ is the nondimensional time variable. Using (21) in (19) and (20), we have

$$\begin{aligned} &\left(1 + \frac{1}{\beta}\right) A_1 \left[\frac{\partial^3 f}{\partial \eta^3} - \frac{1}{\mathrm{Da}}\left(\frac{\partial f}{\partial \eta} - 1\right)\right] \\ &\quad + A_2\left[f\frac{\partial^2 f}{\partial \eta^2} - \left(\frac{\partial f}{\partial \eta}\right)^2 - \frac{\partial^2 f}{\partial \tau \partial \eta} + 1\right] - F_r\left(\frac{\partial f}{\partial \eta} - 1\right)^2 = 0, \end{aligned} \tag{22}$$

$$\begin{aligned} &\frac{A_3}{\mathrm{Pr}}\frac{\partial^2 \theta}{\partial \eta^2} + A_4\left(f\frac{\partial \theta}{\partial \eta} - \frac{\partial f}{\partial \eta}\theta\right) + A_1\, Ec\left(1 + \frac{1}{\beta}\right) \\ &\quad \times \left[\left(\frac{\partial^2 f}{\partial \eta^2}\right)^2 + \frac{1}{\mathrm{Da}}\left(\frac{\partial f}{\partial \eta} - 1\right)^2\right] + \mathrm{Ec}\, F_r\left(\frac{\partial f}{\partial \eta} - 1\right)^3 \\ &\quad - A_4\frac{\partial \theta}{\partial \tau} = 0, \end{aligned} \tag{23}$$

with the boundary conditions

$$\begin{aligned} f(0, \tau) &= S, \\ \frac{\partial f}{\partial \eta}(0, \tau) &= \lambda + \delta\left(1 + \frac{1}{\beta}\right)\frac{\partial^2 f}{\partial \eta^2}(0, \tau), \\ \frac{\partial \theta}{\partial \eta}(0, \tau) &= Bi[\theta(0, \tau) - 1], \\ \frac{\partial f}{\partial \eta}(\infty, \tau) &\longrightarrow 1, \theta(\infty, \tau) \longrightarrow 0. \end{aligned} \tag{24}$$

In order to test the stability of solutions of $f(\eta) = f_0(\eta)$ and $\theta(\eta) = \theta_0(\eta)$ that satisfy boundary value problems (11)–(13), we have

$$\left.\begin{aligned} f(\eta, \tau) &= f_0(\eta) + e^{-\varepsilon\tau} F(\eta, \tau) \\ \theta(\eta, \tau) &= \theta_0(\eta) + e^{-\varepsilon\tau} G(\eta, \tau) \end{aligned}\right\}, \tag{25}$$

where ε is an unknown eigenvalue parameter (a small disturbance of growth or decay) that provides an infinite set of the

eigenvalues $\varepsilon < \varepsilon_1 < \varepsilon_2 < \varepsilon_3 < \ldots$, and $F(\eta, \tau)$ and $G(\eta, \tau)$ are small relative to $f_0(\eta)$ and $\theta_0(\eta)$, respectively. The following linearized problem will be obtained by substituting (25) into (22)–(24).

$$\left(1+\frac{1}{\beta}\right)A_1\frac{\partial^3 F}{\partial\eta^3}+A_2 f_0\frac{\partial^2 F}{\partial\eta^2}-\left(\frac{A_1}{\mathrm{Da}}\left(1+\frac{1}{\beta}\right)+2(A_2+F_r)\frac{\partial f_0}{\partial\eta}\right)\times\frac{\partial F}{\partial\eta}+[A_2\varepsilon+2F_r]\frac{\partial F}{\partial\eta}+A_2\frac{\partial^2 f_0}{\partial\eta^2}F-A_2\frac{\partial^2 F}{\partial\tau\partial\eta}=0, \tag{26}$$

$$\frac{A_3}{\mathrm{Pr}}\frac{\partial^2 G}{\partial\eta^2}+A_4 f_0\frac{\partial G}{\partial\eta}+A_4\left(\varepsilon-2\frac{\partial f_0}{\partial\eta}\right)G+2A_1\mathrm{Ec}\left(1+\frac{1}{\beta}\right)\times\frac{\partial^2 f_0}{\partial\eta^2}\frac{\partial^2 F}{\partial\eta^2}+\left[\frac{2A_1\mathrm{Ec}}{Da}\left(1+\frac{1}{\beta}\right)\left(\frac{\partial f_0}{\partial\eta}-1\right)+3\mathrm{EcFr}\left(\frac{\partial f_0}{\partial\eta}-1\right)^2-2A_4\theta_0\right]\frac{\partial F}{\partial\eta}+A_4\frac{\partial\theta_0}{\partial\eta}F-A_4\frac{\partial G}{\partial\tau}=0, \tag{27}$$

subjected to the boundary conditions

$$F(0,\tau)=0,\ \frac{\partial F}{\partial\eta}(0,\tau)=\delta\left(1+\frac{1}{\beta}\right)\frac{\partial^2 F}{\partial\eta^2}(0,\tau),\ \frac{\partial G}{\partial\eta}(0,\tau)=Bi\,G(0,\tau),\quad \frac{\partial F}{\partial\eta}(\infty,\tau)\longrightarrow 0, G(\infty,\tau)\longrightarrow 0. \tag{28}$$

Following Weidman et al. [43], the initial growth or decay of the solution (25) can be identified by obtaining the steady state solution setting $\tau = 0$ so that $F = F_0(\eta)$ and $G = G_0(\eta)$ in Equations (26)–(28), where $0 < F_0(\eta) \ll 1$ and $0 < G_0(\eta) \ll 1$. The stability of the solution depends upon the sign of the smallest eigenvalue ε. If the value of ε_1 is positive, that shows the flow is stable, and there is an initial decay. Conversely, if the value of ε is negative, that shows the flow is unstable and illustrates an initial growth of disturbance. The linearized eigenvalue problem is given by

$$\left(1+\frac{1}{\beta}\right)A_1F_0'''+A_2f_0F_0''+-\left(\frac{A_1}{\mathrm{Da}}\left(1+\frac{1}{\beta}\right)+2(A_2+F_r)f_0'\right)F_0'+A_2\varepsilon+2F_r+A_2f_0''F_0=0, \tag{29}$$

$$\frac{A_3}{\mathrm{Pr}}G_0''+A_4f_0G_0'+A_4(\varepsilon-2f_{0'})G_0+2A_1\mathrm{Ec}\left(1+\frac{1}{\beta}\right)f_0''F_0''+\left[\frac{2A_1\mathrm{Ec}}{\mathrm{Da}}\left(1+\frac{1}{\beta}\right)\left(f_0'-1\right)+3\mathrm{EcFr}\left(f_0'-1\right)^2-2A_4\theta_0\right]F_0'+A_4\theta_0'F_0=0, \tag{30}$$

subjecting to boundary conditions

$$\begin{aligned}&F_0(0)=0,\\&F_0(0)=0,\\&F_0'(0)=\delta\left(1+\frac{1}{\beta}\right)F_0''(0),\\&G_0'(0)=Bi\,G_0(0),\\&F_0'(\infty)\longrightarrow 0, G_0(\infty)\longrightarrow 0.\end{aligned} \tag{31}$$

To obtain the smallest eigenvalues, there is a need to relax one of the boundary conditions in the form of the initial condition as suggested by Harris et al. [32]. In this problem, $F_0'(\infty) \longrightarrow 0$ has been relaxed in the initial form as $F_0''(0) = 1$. The smallest negative eigenvalues point out the initial development of the disturbance, and the solution of the flow is unstable. On the other hand, the smallest positive related eigenvalue value shows the fluid flow is stable and physically realizable. Thus, the modified boundary conditions (31) become

$$\begin{aligned}&F_0(0)=0,\\&F'(0)=\delta\left(1+\frac{1}{\beta}\right)F_0''(0),\\&G_0'(0)=Bi\,G_0(0),\\&F_0''(0)=1,\\&F_0'(\infty)\longrightarrow 0,\\&G_0(\infty)\longrightarrow 0.\end{aligned} \tag{32}$$

Equations (29) and (30) of linear eigenvalue problem are solved with the boundary conditions (31).

3. Numerical Method

To solve (11) and (12) along with the boundary condition (13) numerically, we use the method of fourth-fifth order using the shooting method with the MAPLE software. In order to apply the solver, first, we reduce the system as a set of equivalent ordinary differential equations of first order using the substitutions $y(1) = f$ and $y(4) = \theta$ as below

$$\begin{aligned}&y(1)'=f'=y(2),\\&y(1)'=f'=y(2),\\&y(2)'=f''=y(3),\end{aligned}$$

$$y(3)' = f''' = \frac{1}{\mathrm{Da}}(y(2)-1) - \frac{1}{(1+(1/\beta))} \cdot \left\{\frac{A_2}{A_1}\left[y(1)y(3) - (y(2))^2 + 1\right] - \frac{F_r}{A_1}(y(2)-1)^2\right\},$$

$$y(4)' = \theta' = y(5),$$

$$y(5)' = \theta'' = -\frac{\mathrm{Pr}}{A_3}\left\{A_4[y(1)y(5) - 2y(2)y(4)] + A_1\,\mathrm{Ec}\left(1+\frac{1}{\beta}\right) \cdot \left[(y(3))^2 + \frac{1}{Da}(y(2)-1)^2\right] + \mathrm{Ec}\,F_r(y(2)-1)^3\right\}. \tag{33}$$

For the boundary conditions (13),

$$\begin{aligned} &\mathrm{ya}(1) = S,\\ &\mathrm{ya}(2) = \lambda + \delta\left(1+\frac{1}{\beta}\right)k_1,\\ &\mathrm{ya}(3) = k_1,\\ &\mathrm{yb}(2) = 1,\\ &\mathrm{ya}(4) = k_2,\\ &\mathrm{ya}(5) = Bi[k_2 - 1],\\ &\mathrm{yb}(4) = 0. \end{aligned} \tag{34}$$

To do stability analysis, we follow the same procedures. New substitutions are introduced to rewrite Equations (29) and (30) and the boundary conditions (32) into first order ordinary differential equations, by letting $y(1) = F_0$, $y(4) = G_0$, $z(1) = f_0$, and $z(4) = \theta_0$.

$$y(1)' = F_0' = y(2),$$
$$y(2)' = F_0'' = y(3),$$

$$y(3)' = F_0''' = \frac{1}{A_1(1+(1/\beta))}\left\{\left[\frac{A_1}{\mathrm{Da}}\left(1+\frac{1}{\beta}\right) + 2(A_2+F_r)z(2) - (A_2\varepsilon + 2F_r)\right]y(2) - A_2[z(1)y(3) + y(1)z(3)]\right\},$$

$$y(4)' = G_0' = y(5),$$

$$y(5)' = G_0'' = -\frac{\mathrm{Pr}}{A_3}\left\{A_4[[z(1)y(5) + z(5)y(1) + \varepsilon y(4)] - 2[y(2)z(4) + z(2)y(4)]] + 2A_1\,\mathrm{Ec}\left(1+\frac{1}{\beta}\right)y(3)z(3) + \left[\frac{2A_1\mathrm{Ec}}{Da}\left(1+\frac{1}{\beta}\right)(z(2)-1) + 3\mathrm{Ec}\,F_r(z(2)-1)^2\right]y(2)\right\}. \tag{35}$$

For the boundary conditions,

$$\begin{aligned} &\mathrm{ya}(1) = 0,\\ &\mathrm{ya}(2) = \delta\left(1+\frac{1}{\beta}\right)k_1,\\ &\mathrm{ya}(3) = k_1,\\ &\mathrm{yb}(2) = 0,\\ &\mathrm{ya}(4) = k_2,\\ &\mathrm{ya}(5) = Bi\,k_2,\\ &\mathrm{ya}(3) = 1,\\ &\mathrm{yb}(4) = 0,\\ &\mathrm{za}(1) = S,\\ &\mathrm{za}(2) = \lambda + \delta\left(1+\frac{1}{\beta}\right)l_1,\\ &\mathrm{za}(3) = l_1,\\ &\mathrm{zb}(2) = 1,\\ &a(4) = l_1,\\ &\mathrm{za}(5) = Bi[l_2 - 1],\\ &\mathrm{zb}(4) = 0. \end{aligned} \tag{36}$$

To determine the unknown initial conditions k_1, k_2, l_1, and l_2, we shoot them for arbitrary slope so that the solution of the system of ODEs satisfies the boundary conditions at ∞, and its accuracy is checked by comparing the calculated quantities with the provided end points. After obtaining these values, we apply the fourth-fifth order Runge-Kutta-Fehlberg technique to solve a system of first-order ODEs in (33) with boundary conditions (34) and determine ε from (35). To get the dual solutions, we take different initial approximates for the values of k_1, k_2,where all profiles asymptotically satisfy the ∞ boundary conditions.

4. Results and Discussion

In this study, the results of the combined effects of velocity ratio (stretching/shrinking) parameter λ, Casson's parameter (factor) β, Darcy's number Da, Forchheimer's (porous medium inertia) parameter F_r, suction/injection parameter S, velocity slip (slipperiness) parameter δ, Prandtl's number Pr, Eckert's number Ec, Biot's number Bi, and the nanoparticle volume fraction ϕ on the fluid flow temperature and velocity profiles are demonstrated using plots, and computations are made for these embedded parameters. The range of parameters considered in the study is $0.0 \le \phi \le 0.1, 0.1 \le \beta \le 10, 0.1 \le \mathrm{Da} \le 20, 0.1 \le \mathrm{Fr} \le 5, 0.02 \le S \le 0.5, 0.1 \le \delta \le 0.5, 0.1 \le \mathrm{Ec} \le 0.3, 0.05 \le \mathrm{Bi} \le 0.15$. Since the single phase

Table 2: Comparison of values of skin friction $\sqrt{\mathrm{Re}_x}C_f$ for varying values of stretching/shrinking parameter λ with $\phi = 0$, $\beta = Da = \infty$, $Fr = S = \delta = 0$.

λ	Nazar et al. [24]	Jumana et al. [27]	Tadesse et al. [37]	Present result
-0.25	1.40224	—	1.402241	1.402240800
0	1.232588	1.232587	1.232588	1.232587800
0.2	1.05113	1.051129	1.051130	1.051129994
0.5	0.71329	0.713295	0.713295	0.713294956
1	0	0.000000	0	0

nanofluid flow model under investigation is a water base with Copper nanoparticles, the effective Prandtl number of working nanofluid is that of pure water (i.e. Pr = 6.2) by Shaw et al. [34] and Joshi et al. [36], whereas the universal values of parameters used in the present study are as follows: $\beta = 10$, Pr = 6.2, $\phi = \mathrm{Da} = \mathrm{Fr} = S = \delta = \mathrm{Ec} = \mathrm{Bi} = 0.1$. In addition, the occurrence of two solutions for certain ranges of parameter variations is demonstrated for the coefficient of skin friction C_f and Nusselt number (rate of heat transfer) Nu_x in graphs and/or tables for diverse numerical quantities of parameters. The existence of dual solutions due to shrinking surface for certain ranges of parameter variations is shown for the skin friction coefficient using graphs and tables, and also, the variations of Nusselt's numbers are demonstrated in graphs for different values of change of parameters. The governing nonlinear ordinary differential equations, Equations (11) and (12), with the boundary conditions (13) are solved numerically using shooting techniques built-in Maple2018 software. The MAPLE solver has been used widely by many researchers to solve the boundary value problem (BVP), and this solver is coded with a finite difference in fourth order accuracy level. To validate this method, we compare the computational results obtained with that of the coefficient of skin friction of preceding works given by Nazar et al. [24], Jumana et al. [27], and Tadesse et al. [37], as presented in Table 2. It is observed that there is a nice agreement, and hence, the method is proper for tackling problems of the current study. The velocity and temperature profiles as well as skin friction and Nusselt's number are graphically presented.

4.1. Existence of Dual Solutions due to Shrinking Sheet. In Figures 2–4, the impacts of different values of the involving parameters on the skin friction for shrinking parameter λ are presented. These figures demonstrate that dual solutions exist with upper (solid curve) and lower (dotted curve) branches for $\lambda > \lambda_c$ and no real solution for $\lambda < \lambda_c$. For shrinking parameter λ, the critical value λ_c is the quantity where the upper and lower branch solutions meet each other. In other words, physically λ_c shows the extent to which the sheet surface can shrink while processing. From these figures, it is observed that $|\lambda_c|$ enhances with S and δ and decreases with increasing values of ϕ, β, Da, and Fr. That means the interval of the shrinking parameter λ for which the similarity solution exists widens as suction and slipperiness of the surface parameters increase, whereas it diminishes as the Casson factor, nanoparticle volume fraction, porous medium, and porous medium inertia parameters increase. On the other side of this critical value λ_c, no similar solutions exist because of the boundary layer separation from the surface of the sheet, and it is not possible to get the solution using the boundary layer approximations. In Figure 2(a), we see that for the upper branch solution for the shrinking parameter λ, the value of the skin friction coefficient (surface drag force) lessened with a rise in nanoparticle volume fraction ϕ and reversed as it approached the critical value of the shrinking parameter. In reality, the rising nanoparticle volume fraction means that the nanoparticles and the base fluid collide with each other, which raises the motion of the nanofluid; as a result, the thickness of the momentum boundary layer diminishes and increases the surface drag force. This result agrees with the computed and tabulated values in Table 3. For $\lambda = 1$, we always obtain $f''(0) = 0$ for all values of ϕ since the fluid velocity is the same as velocity of the stretching/shrinking surface of the sheet. In Figure 2(b), we see that the skin friction coefficient diminishes as the Casson factor β increases for the upper branch solution. This is due to an increment in β, which means that the fluid loses its non-Newtonian behavior and acts like a Newtonian type, and hence, its velocity enhances, resulting in the reduction of shear stress. Figures 3(a) and 3(b) illustrate the coefficient of skin friction reduces by intensifying values of porous medium parameter Da and porous medium inertia parameter Fr. As demonstrated in Figure 4(a), the coefficient of skin friction augments with increasing values of suction parameter S for the upper branch solution, since suction at the boundary surface retards flow of the fluid and increases the coefficient of skin friction. Figure 4(b) also demonstrates the skin friction for the shrinking case, and it is observed that for the upper branch solution, the surface drag force diminished with a rise in slipperiness parameter δ and reversed as it approached the critical value of the shrinking parameter. All these results in Figures 2(b)–4(b) best agree with the numerical results in Table 4. Figure 5 demonstrates the presence of a dual solution using the graph of local Nusselt's number Nu_x, by taking particular numerical values of viscous dissipation parameter Ec and convective heating parameter Bi, to observe their impact on the process of heat transfer and the intervals of dual solution existence, for the shrinking sheet. It is noted from the model that the energy and momentum equations are coupled and hence the Nusselt number characterizes a dual solution for $\lambda_c < \lambda < 0$ in the case of a shrinking sheet surface as displayed for particular governing parameters in figures. In Figure 5(a), it is observed that as viscous dissipation parameter Ec increases, the local Nusselt number enhances for the upper branch solution and drops for lower branch solutions, where the upper branch solution is the one which is stable and physically realizable, while the lower branch solution is not. Thus, minimum viscous dissipation (minimum Ec) is an acceptable sign for the rate of heat transfer enhancement of the nanofluid as the literature reveals. The interval of solution widens as the viscous dissipation Ec escalates. Again, Figure 5(b) reveals that as convective heating parameter Bi increases, the local Nusselt number rises for both the upper and lower

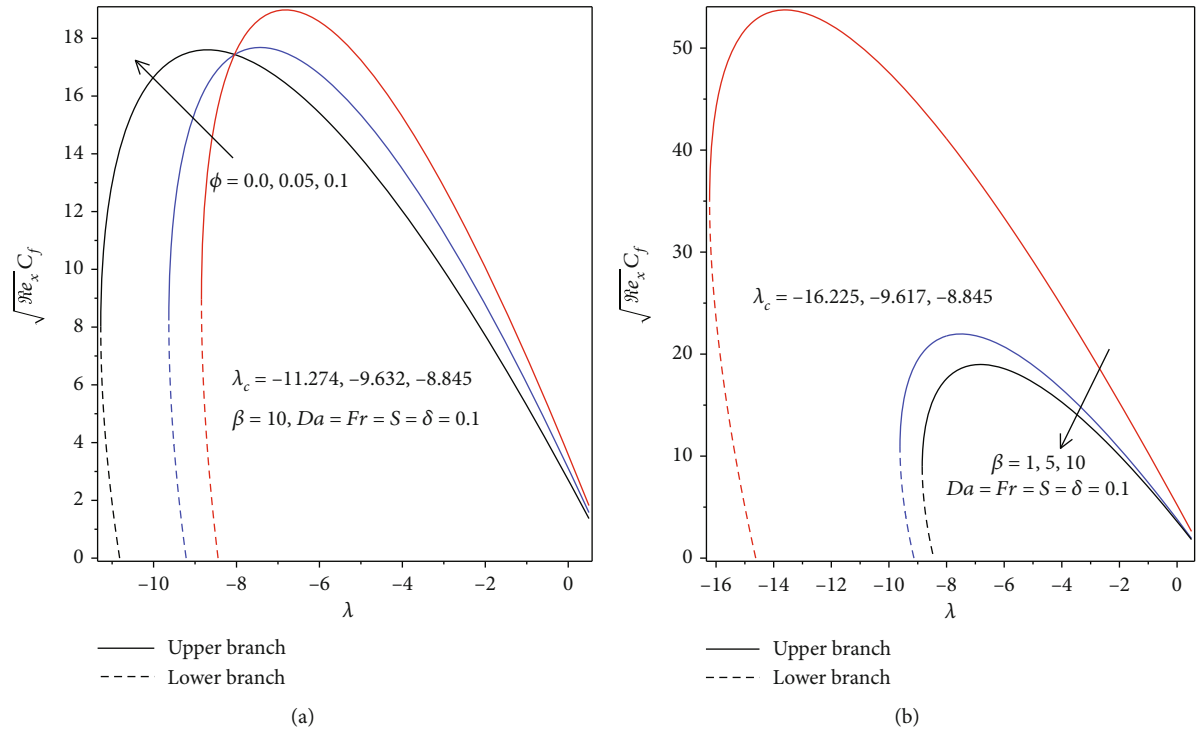

Figure 2: Shrinking parameter λ versus skin friction for varying values of (a) ϕ and (b) β.

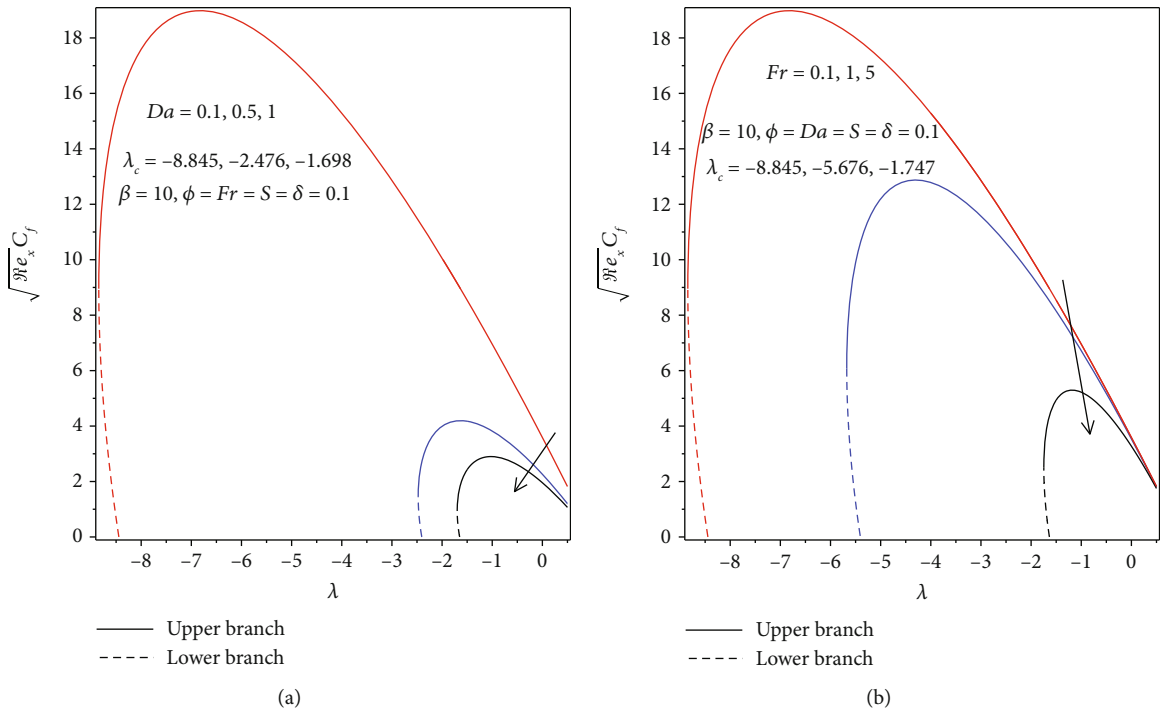

Figure 3: Shrinking parameter λ versus skin friction for varying values of (a) Da and (b) Fr.

branch solutions for shrinking sheet surface. That means, the coefficient of heat transfer caused by the hot fluid beneath the sheet is directly associated with the convective heating parameter. However, unlike the viscous dissipation parameter case, the interval of existence of the dual solution gets narrowed for increasing convective heating parameters.

4.2. Velocity Profile. Figures 6 and 7 present the impacts of different values of velocity ratio (stretching/shrinking) parameter λ, Casson's parameter(factor) β, Darcy's number (porous media) Da, Forchheimer's (porous medium inertia) parameter F_r, suction/injection parameter S, velocity slip (slipperiness) parameter δ, and nanoparticle volume fraction

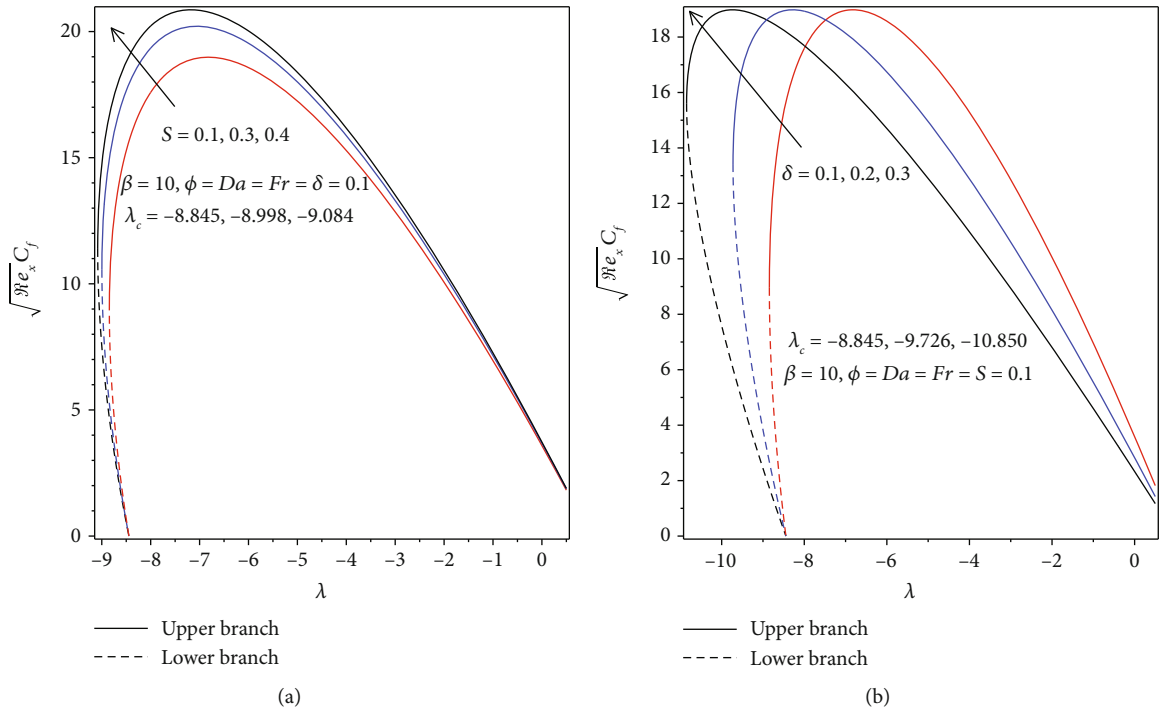

Figure 4: Shrinking parameter λ versus skin friction for varying values of (a) S and (b) δ.

Table 3: The computation showing critical shrinking parameter, skin friction, and the smallest eigenvalues for both upper and lower solutions for varying values of ϕ and λ when $\beta = 10$, Da = Fr = $S = \delta = 0.1$ for Cu-H_2O nanofluid.

Varying parameters			$\sqrt{Re_x}C_f$		ε	
ϕ	λ_c	λ	Lower branch	Upper branch	Lower branch	Upper branch
		-11.245	6.1226218	9.7873344	-1.8948508	0.2557403
0	-11.274	-11.250	6.2977932	9.6332684	-1.7985628	0.1584437
		-11.255	6.4913428	9.4608324	-1.6915341	0.0504055
		-9.610	6.4645936	9.8859367	-1.4190913	0.2465134
0.05	-9.632	-9.614	6.6359242	9.7343401	-1.3409342	0.1672097
		-9.617	6.7765913	9.6084782	-1.2764123	0.1018277
		-8.821	6.8970069	10.8728661	-1.4272733	0.2188636
0.1	-8.845	-8.826	7.1259643	10.6726304	-1.3390939	0.1290218
		-8.831	7.3851530	10.4421769	-1.2384452	0.0267103

ϕ on fluid velocity profile for the upper branch solution (for the stable upper branch solution only). Figure 6(a) displays the effect of the Casson factor β on the velocity profile. It is revealed that initially, the velocity profile and the flow boundary layer thickness decrease with increasing β, but after a certain distance from the stretching sheet surface, the velocity profile starts to enhance with increasing β. It is observable that the fluid velocity is minimal near the sheet surface, but it tends to be high as far away from the sheet surface. The main cause for getting such a result is that the augmented Casson's factor reduces the yield stress (fluid behaves like a Newtonian one when Casson's factor becomes very large) which, in turn, restraints the velocity of the Cu-H_2O-Casson nanofluid. Here, for all Casson's factor β, $f'(\eta)$ is an increasing function of η. It is also important to note that when the values of β indefinitely inflate ($\beta \longrightarrow \infty$), the non-Newtonian property of the Casson fluid goes, and it acts like a Newtonian fluid flow, and hence, the flow boundary layer thickness of the Cu-H_2O-Casson nanofluid drops, and the velocity profile increases far from the surface of the sheet. This also happened due to the plastic viscosity of the Casson fluid, which is inversely proportional to the Casson factor. From the same figure, it is observed that an increment in the velocity ratio parameter λ resulted in the enhancement of the flow velocity profile and its boundary layer thickness. In Figure 6(b), it is observed that diminutive velocity profiles $f'(\eta)$ are observed in response to increment in porous media parameter Da on the boundary layer flow of the Cu-H_2O-Casson nanofluid. This is due to the presence of more and more porous matrix producing more and more resistant forces that contribute to more and more retarded flow and

Table 4: The computation showing impact of parameters variation on critical shrinking parameter, skin friction, and the smallest eigenvalues for both upper and lower solutions for Cu-H_2O nanofluid when $\phi = 0.1$ is fixed.

							$\sqrt{Re_x}C_f$		ε	
β	Da	Fr	S	δ	λ_c	λ	Lower B	Upper B	Lower B	Upper B
10	0.1	0.1	0.1	0.1	-8.845	-8.821	6.897006	10.872865	-1.427273	0.218863
5	0.1	0.1	0.1	0.1	-9.617	-9.601	9.095182	12.600703	-1.252935	0.108050
1	0.1	0.1	0.1	0.1	-16.225	-16.211	32.431338	37.553862	-1.044620	0.396915
10	0.5	0.1	0.1	0.1	-2.476	-2.440	0.428272	2.368089	-1.375845	0.027543
10	1	0.1	0.1	0.1	-1.698	-1.650	0.004414	1.765601	-1.444670	0.097651
10	0.1	1	0.1	0.1	-5.676	-5.550	2.035769	9.389230	-4.281724	1.600540
10	0.1	5	0.1	0.1	-1.747	-1.700	0.929175	3.800993	-0.491905	8.418994
10	0.1	0.1	0.3	0.1	-8.998	-8.971	8.431013	12.530511	-1.368711	0.331972
10	0.1	0.1	0.4	0.1	-9.084	-9.070	9.872623	12.811560	-1.087406	0.131775
10	0.1	0.1	0.1	0.2	-9.726	-9.712	12.336980	14.416381	-0.757477	0.349037
10	0.1	0.1	0.1	0.3	-10.850	-10.810	14.224548	16.739973	-0.870792	0.845219

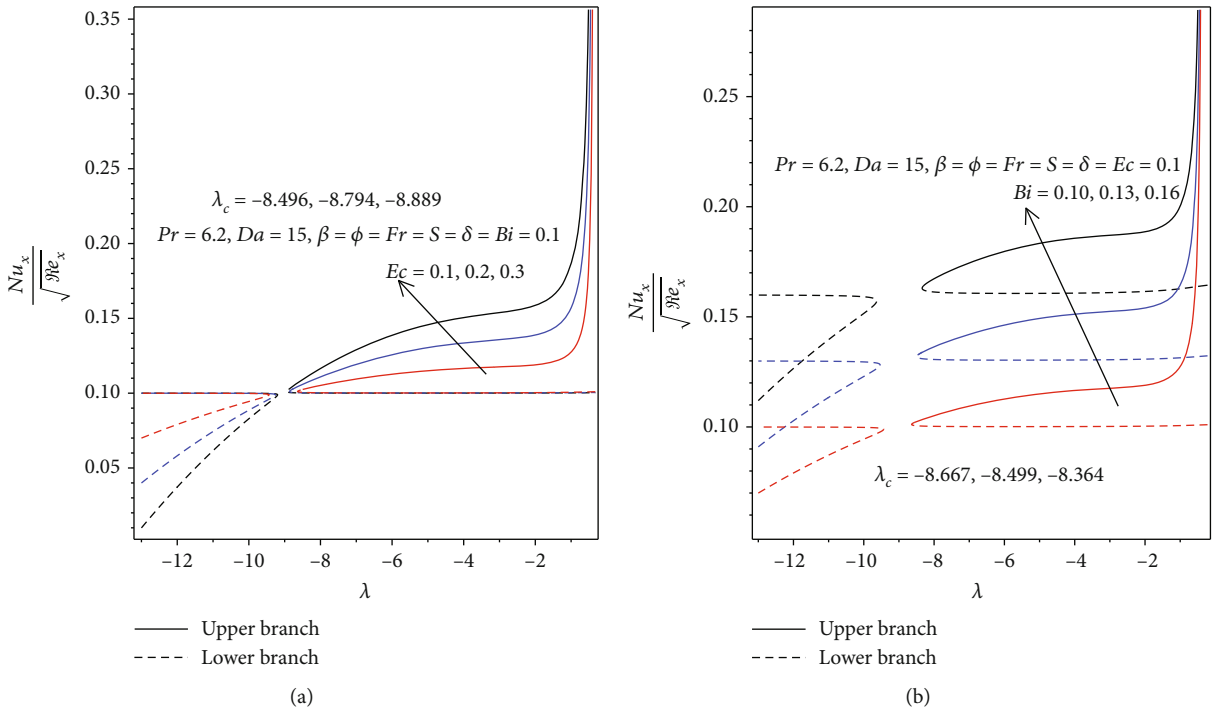

Figure 5: (a) Change in the local Nusselt's number for shrinking sheet with *Ec*. (b) Change in the local Nusselt's number for shrinking sheet with *Bi*.

shrinking of the corresponding boundary layer thickness. This figure again describes how the porous medium inertia parameter Fr engulfs the velocity profile $f'(\eta)$ within the flow regime. Thus, the increment in porous media inertial resistance looms the velocity profile and the related reduced boundary layer thickness. Figure 7(a) depicts that intensifying the values of Cu-H_2O volume fraction ϕ increases the velocity of the flow. That is, the higher ϕ augments the velocity profile due to the spherical-shape of Cu nanoparticle. Physically, the higher ϕ enhances the motion of the spherical-shaped the Cu nanoparticles which diminishes the boundary layer thickness and raises the velocity profile of the Cu-H_2O-Casson nanofluid flow. The same figure also shows that improving the value of suction S augments the velocity of the flow, which is because suction is dominated by slipperiness of the surface and reduces the drag on the surface to control the separation of the boundary layer. As the slipperiness parameter δ rises, the velocity profile escalates, whereas its boundary layer thickness diminishes as demonstrated in Figure 7(b).

4.3. Temperature Profile. The effects of different values of the parameters: velocity ratio (stretching/shrinking) parameter λ, Casson's factor β, Darcy's number Da, Forchheimer's (porous medium inertia) parameter F_r, suction/injection parameter S, velocity slip (slipperiness) parameter δ, Prandtl's number Pr,

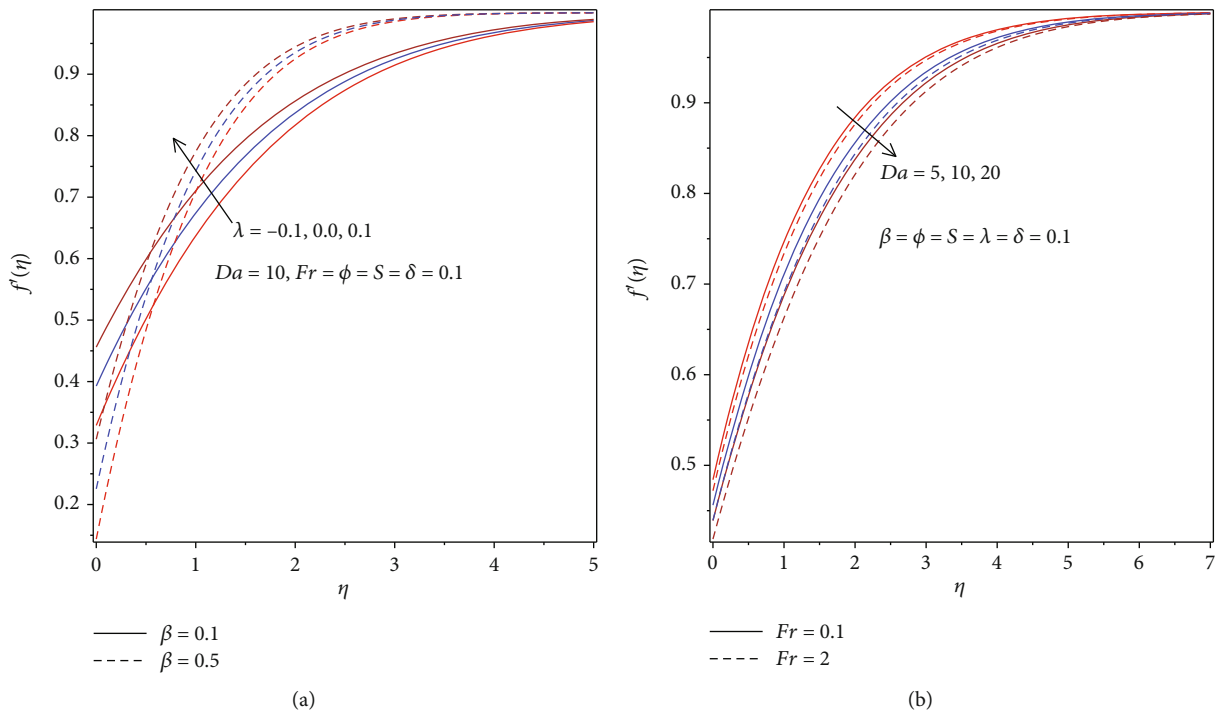

FIGURE 6: (a) Velocity profile with λ and β for the upper branch solution. (b) Velocity profile with Da and Fr for the upper branch solution.

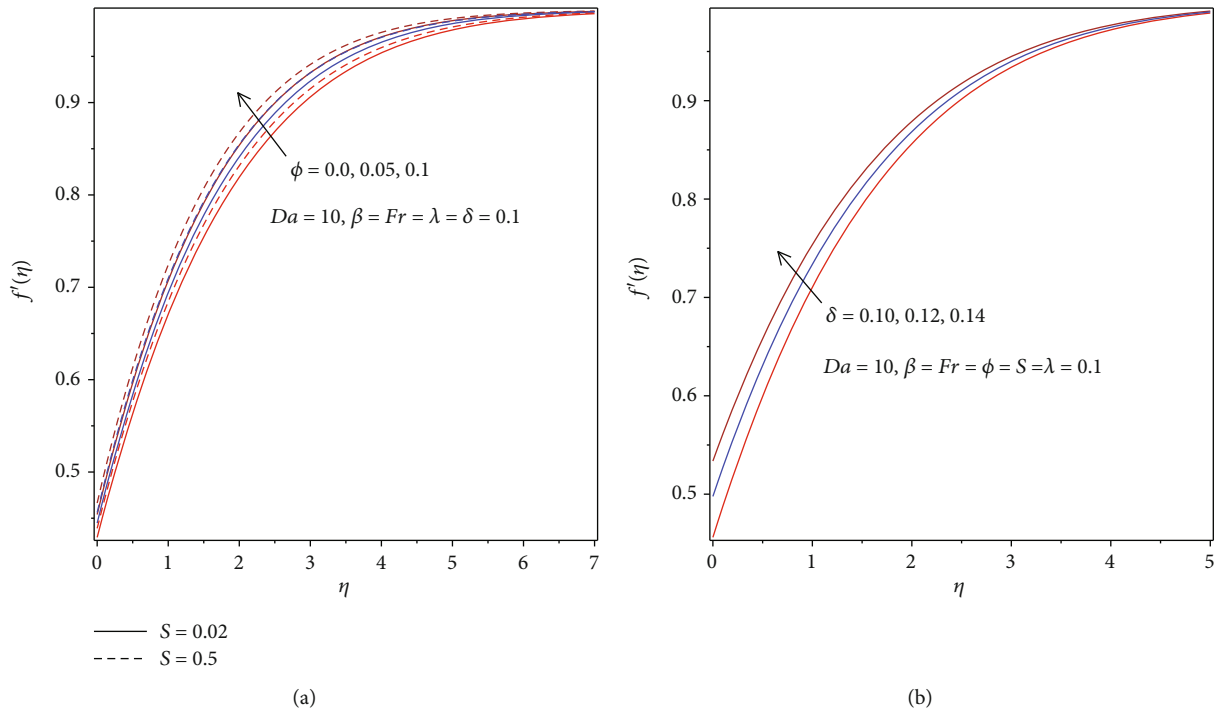

FIGURE 7: (a) Velocity profile with ϕ and S for the upper branch solution. (b) Velocity profile with δ for the upper branch solution.

Eckert's number Ec, Biot's number Bi, and nanoparticle volume fraction ϕ on fluid temperature profile for the upper branch solution were demonstrated in Figures 8–10(a). In Figure 8(a), it is observed that the temperature profiles are belittled for enhancing values of the Casson factor β. As the Casson factor values get higher, the yield stress strength of Cu-H_2O-Casson nanofluid weakens, which, in turn, enhances the plastic dynamic viscosity, and therefore, the thickness of the thermal boundary layer diminishes, for raising values of the Casson factor β. Here, we note that the Cu-H_2O-Casson nanofluids thermal boundary layer thickness is greater than that of the Newtonian fluid. We know that as the values of the Casson factor get higher ($\beta \longrightarrow \infty$), the Cu-$H_2O$-Casson nanofluids act as a Newtonian fluid. Therefore, reducing stress

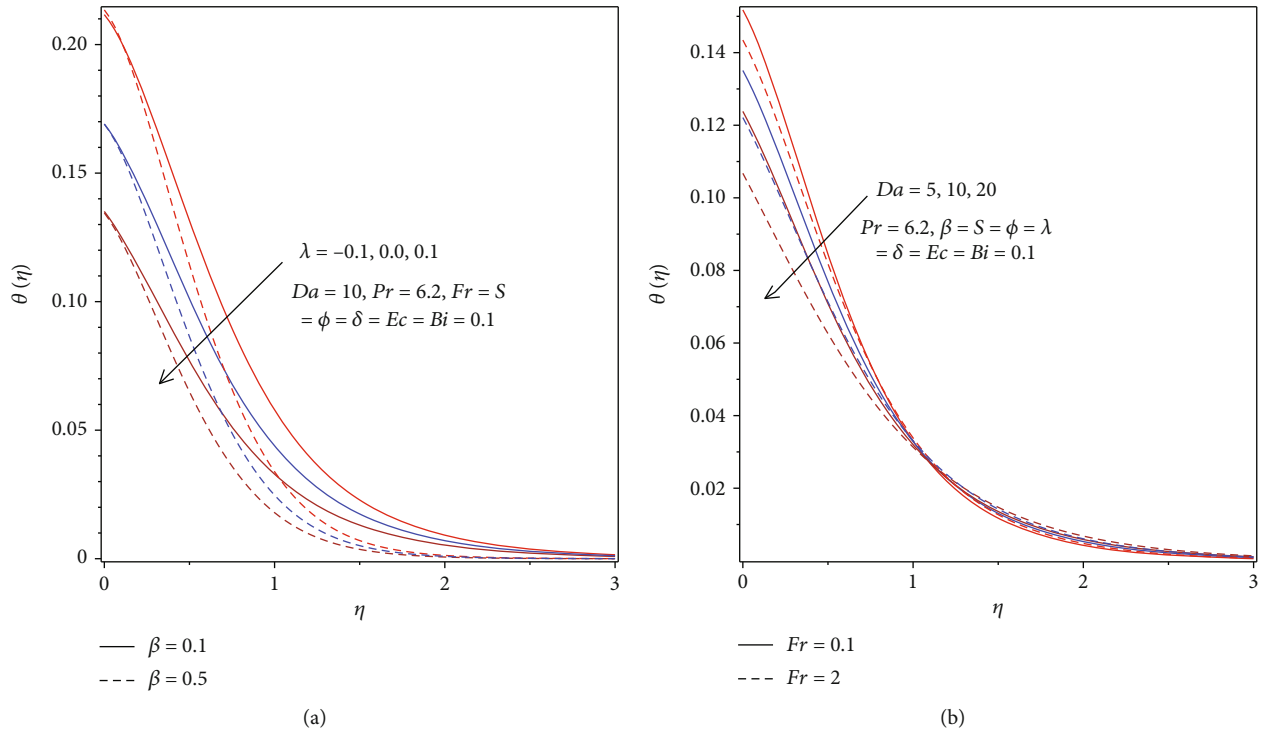

Figure 8: (a) Temperature profile with λ and β for the upper branch solution. (b) Temperature profile with Da and Fr for the upper branch solution.

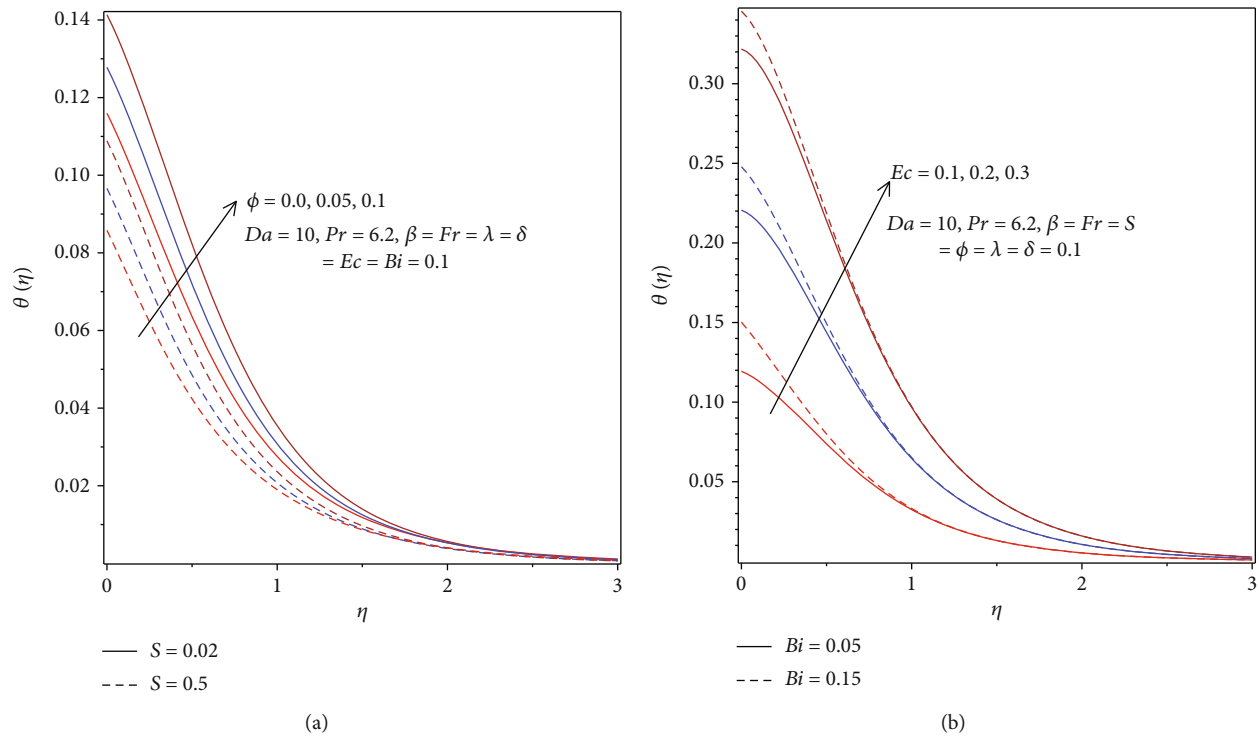

Figure 9: (a) Temperature profile with ϕ and S for the upper branch solution. (b) Temperature profile with Ec and Bi for the upper branch solution.

escalates the fluid flow and drops its heat transfer. The same figure also illustrates that an increment in the velocity ratio λ resulted in a diminishing of the temperature profile of the Cu-H_2O-Casson nanofluid flow, which shows that stretching of the surface tends to squeeze the thermal boundary layer of the Cu-H_2O-Casson nanofluid flow. The temperature profile

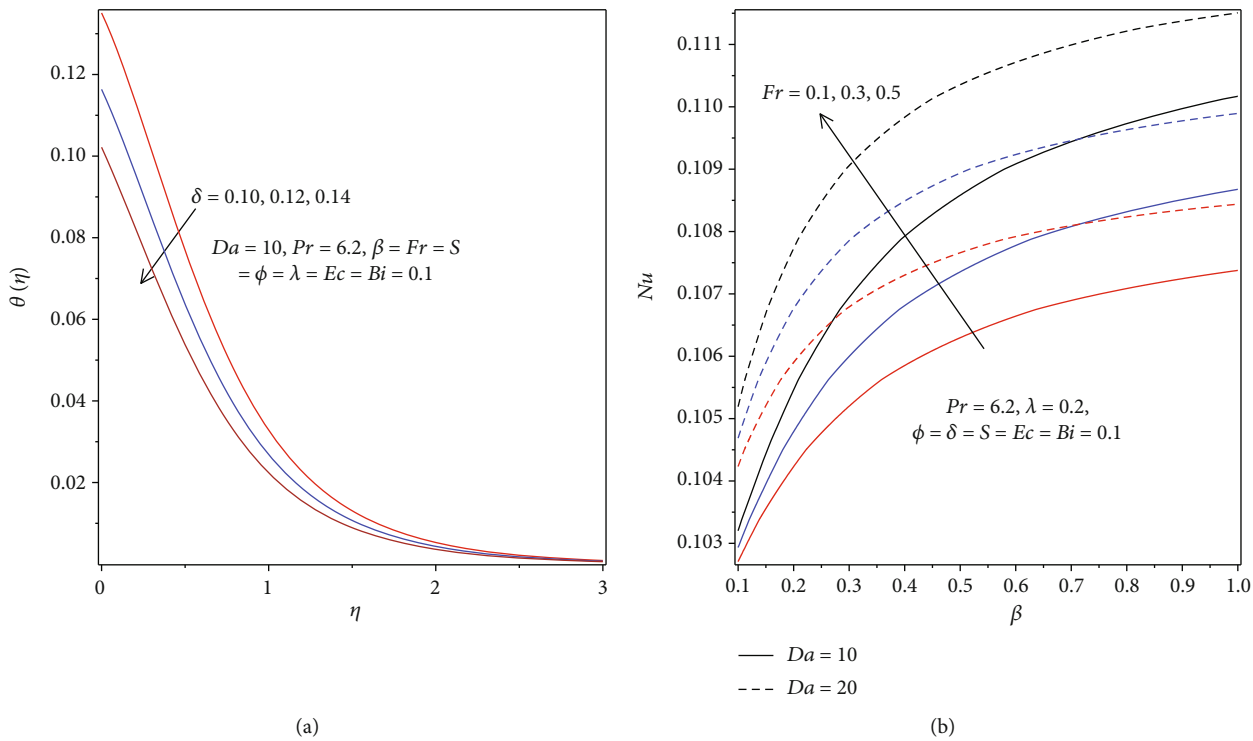

FIGURE 10: (a) Temperature profile with δ for the upper branch solution. (b) β versus Nu for varying values of Da and Fr.

due to the porous medium parameter Da is demonstrated in Figure 8(b). The temperature profile falls due to an increment in Da within a few boundary layers of fluid from the surface of the sheet ($\eta < 1.13$), and beyond ($\eta > 1.13$) the temperature profile switches trend due to an increment in Da. This figure also displays the impact of the nonlinear porous medium inertia parameter Fr on the fluid temperature profile. It is observed that an increment in the porous medium inertia parameter produces the falling fluid temperature profile and the thermal boundary layer. By looking at Figure 9(a), to observe how the temperature profile behaves in dealing with different Cu-H_2O nanoparticle volume fractions ϕ, and it is seen that as ϕ increases, the temperature profile $\theta(\eta)$ and the corresponding thermal boundary layer also increase. Since the Cu nanoparticle has high thermal conductivity, physically, it means increasing nanoparticle volume fraction ϕ upsurges the temperature profile and heat transfer rate. That is, due to enhanced thermal conductivity, Cu nanoparticles heighten the thermal enhancement of the Casson nanofluid past the permeable surface. The same figure reveals that augmented fluid suction parameter S produces both a diminutive temperature profile and its thermal boundary layer thickness. As a result, when impacts of viscous dissipation overrun, for augmenting suction parameter S, the thermal boundary layer thickness diminishes. The distribution of the temperature field gets more consistent within the boundary layer of flow because of the impact of suction. Figure 9(b) illustrates the impact of viscous dissipation (Eckert's number Ec) on temperature profile. There is an indication that an increase in the viscous dissipation parameter is highly beneficial to the growth of temperature profile in the flow region. We know that viscosity absorbs kinetic energy from the fluid motion and changes it into internal energy that improves heating the fluid flow, hence increasing the temperature profile. Moreover, the same figure demonstrates that augmenting the convective heating (increment in Biot number Bi) enhances the temperature profile of Cu-H_2O-Casson nanofluid flow. That means, the coefficient of heat transfer caused by the hot fluid beneath the sheet is directly associated with the convective heating parameter Bi. That is, behavior of temperature profiles due to convective heating is higher near the boundary layer, implicating that the fluid temperature adjacent to the sheet surface surpasses that of the free stream fluid flow. Thus, the increasing convective heating parameter Biresulted in an increment in the convective temperature profile of the fluid flow. In Figure 10(a), it is observed that increasing sheet surface slipperiness δ reduces both the temperature profile and the thermal boundary layer thickness of the Cu-H_2O-Casson nanofluid flow.

4.4. Rate of Heat Transfer. Figure 10(b) reveals that the intensification in the values of the Casson factor β, porous media parameter Da, and porous media inertia parameter Fr resulted in the enhancement of the local Nusselt's number for the stretching sheet. An increment in the Casson factor β raises the fluid motion due to slipperiness and drops the thermal profile, resulting in enhanced heat transfer rate, whereas as the porous media parameter increases, both the fluid motion and the thermal profile diminish, which also enhances the Nusselt number (rate of heat transfer) rate at the stretching sheets surface. Figure 11(a) depicts that the rise in the values of nanoparticle volume fraction ϕ resulted in the rise of the Nusselt number Nu, which in reality means that the rate of heat transfer at the surface of the sheet enhances as nanoparticle volume fraction rises. In other

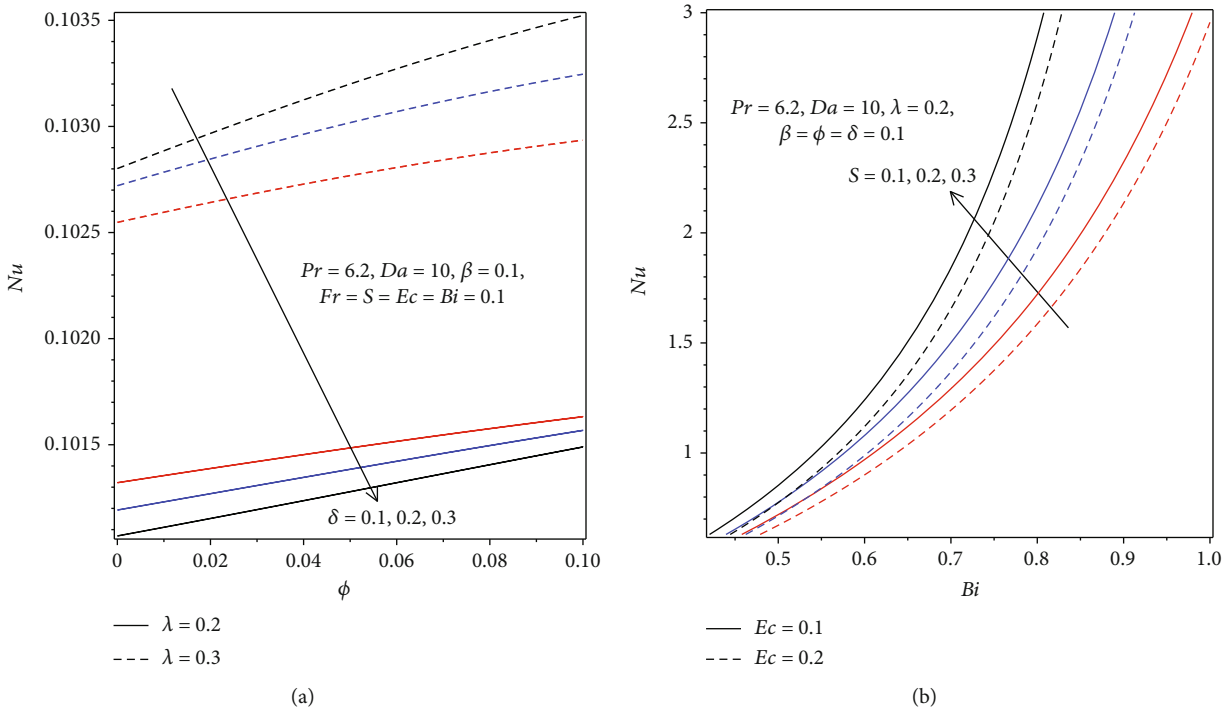

FIGURE 11: (a) ϕ versus Nu for varying values of δ and λ. (b) Bi versus Nu for varying values of S and Ec.

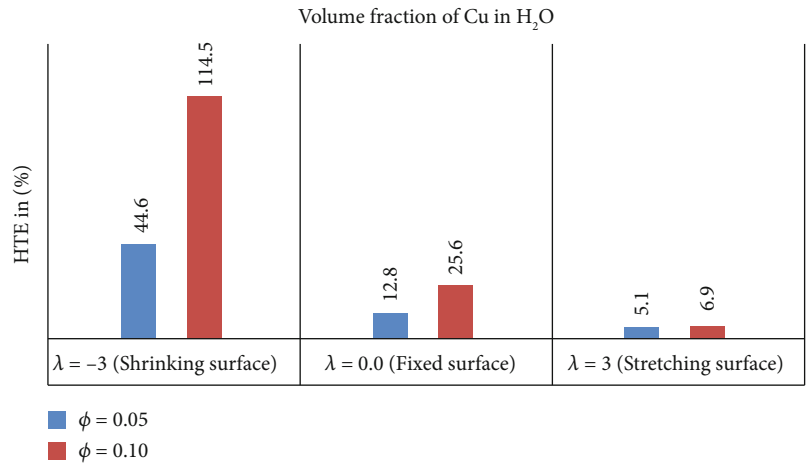

FIGURE 12: Rate of heat transfer enhancement with ϕ for fixed values Pr = 6.2, β = 10, Da = Fr = S = δ = Ec = Bi = 0.1.

words, the addition of the Cu-H_2O nanoparticle volume fraction produces a rise in the temperature gradient at the sheet surface and results in the rate of heat transfer from the surface of the sheet to the fluid. Again, it can be concluded that the heat transfer properties of the Casson fluid becomes better because of the addition of the Cu-H_2O nanoparticles into it. The same figure also revealed that rising in the values of stretching parameter λ resulted in the ascending of the Nusselt number Nu, which means as stretching of the surface increases, the heat transfer at the surface rises. Again, the stepping-up in the values of slip parameter δ reduces the Nusselt number Nu, and hence, the heat transfer rate drops, which is due to improvement in slipperiness of the sheet surface reducing adhesion of the fluid to it, as we see from the same figure. Figure 11(b) explains the impact of suction parameter S, Eckert's number Ec, and Biot's number Bi on the Nusselt number for stretching sheet surfaces. From this figure, it is observed that an increment in suction parameter S boosts the processes of heat transfer rate from the stretching sheet surface, which is due to an increase in the suction rate that raises the Cu-H_2O nanoparticle accumulation on the stretching sheet surface that resulted in an enhancement in heat transfer rate (Nusselt number Nu) of the fluid. In other words, the minimum temperature gradient at the sheet surface is closely linked with an inverse relation to the heat transfer rate from the surface of the sheet. This shows that higher suction parameter S resulted in a considerably higher heat transfer rate. This figure also

illustrates the impact of viscous dissipation on the management of heat transfer from the surface of the sheet. It is observed that the viscous dissipation parameter *Ec* raises the heat transfer rate falls, which is due to the slipperiness of the surface and the addition of nanoparticles, and moreover, the flow motion increases, and hence, the temperature gradient drops, which, in turn, results in an enhanced rate of heat transfer. Due to convective heating of the sheet surface, it is seen that the Nusselt number (heat transfer rate) rises as convective parameter *Bi* augments, as we see from the same figure.

4.5. Heat Transfer Enhancement. The chart in Figure 12 demonstrates how fast heat transfer is enhanced for the increasing values of Cu-H_2O nanoparticle for the Cu-H_2O-Casson nanofluid flow. For the shrinking sheet, taking 10% of the nanoparticle volume fraction, the heat transfer rate is boosted up to 114.5% for Cu-H_2O. Generally, the heat transfer enhancement rate drops from the shrinking sheet towards the stretching sheet surface as observed from the chart. Moreover, the rate of heat transfer enhancement upsurge for working nanofluids with increasing Cu-H_2O nanoparticle volume fraction. Studies revealed that Cu-H_2O nanoparticles serve as a better coolant for industrial and engineering usage when compared to other water-based nanoparticles.

4.6. Numerical Analysis of Stability Test. From the computational results of this problem, the dual solution exists for some interval of λ. Temporal stability analysis is made to determine stable solutions among different solutions appear due to a shrinking sheet surface. As detailed in Table 3, for different values of Cu-H_2O nanoparticle volume fraction ϕ and velocity ratio λ, the smallest eigenvalue ε is calculated for the temporary change of small perturbations regarding the basic steady flow, where the values of $\beta = 10$, $\mathrm{Da} = \mathrm{Fr} = S = \delta = 0.1$ are fixed. Similar calculations were done for fixed $\phi = 0.1$ as presented in Table 4. It is noted that since the value of the smallest eigenvalue ε is positive, the upper branch solution for shrinking sheet surface is hydrodynamically temporally stable and, hence, physically realizable. Clearly, for the lower branch solution, the negative value of ε revealed that it is unstable and physically unrealistic. In addition, $\varepsilon > 0$ demonstrates the rate of declination of small disturbance in the upper branch solution, whereas $\varepsilon < 0$ or the lower branch solution shows the increment of the disturbances.

5. Conclusions

A numerical investigation of boundary layer flow of Cu-H_2O-Casson nanofluid past a slippery stretching/shrinking sheet through a Darcy-Forchheimer porous medium has worked out to demonstrate the overall impacts of Casson's factor, viscous dissipation, suction/injection, convective heating, and porous medium resistance parameters. Using similarity transformations, the modeled boundary layer equations are transformed into a system of ODEs, and the MAPLE software package is used for the computation of the numerical solutions. Stability analysis has been done to identify stable and physically reliable solutions subjected to small perturbations. The effects of various parameters on the dimensionless velocity and temperature profiles, coefficient of skin friction, the rate of heat transfer, and heat transfer enhancement are obtained numerically and presented in graphs, tables, charts. The following findings are derived from the discussions:

(i) There is a critical value of shrinking parameter λ_c below which no real, dual, or unique solutions exist. The critical value $|\lambda_c|$ widens with increase in suction, slipperiness of surface, and viscous dissipation parameters, whereas it diminishes with increase in Cu-H_2O nanoparticle volume fraction, Casson's factor, porous medium, and porous medium inertia parameters

(ii) Temporal stability analysis provided the smallest eigenvalue ε, which revealed that only the upper branch solution is stable and physically realizable, whereas the lower branch solution is unstable and not realistic

(iii) The skin friction (wall shear stress) at the sheet surface increases as nanoparticle volume fraction and suction parameters escalate but reduces with increment in Casson's factor, slipperiness of the sheet, porous medium, and porous medium inertia parameters

(iv) The velocity profile augments with the increment in nanoparticle volume fraction, velocity ratio, and suction and slipperiness parameters. However, it decreases with increasing values of the Casson factor, porous medium, and porous medium inertia parameters for the upper branch solution

(v) Widening of the momentum boundary layer thickness is observed with enhancement in porous medium and porous medium inertia parameters, whereas it diminishes with increment in velocity ratio, suction, slipperiness of surface, Casson's factor, and nanoparticle volume fraction parameters

(vi) The temperature profile and the thermal boundary layer thickness rise with incremental nanoparticle volume fraction, Casson's factor, viscous dissipation, and convective heating, whereas they decrease with increase in velocity ratio, suction, slipperiness, porous medium, and porous medium inertia parameters

(vii) The rate of heat transfer intensifies with the increment in Casson's factor, porous medium, porous medium inertia parameters, suction, velocity ratio, nanoparticle volume fraction, and convective heating parameters but drops with increase in slipperiness of the surface and viscous dissipation parameters

(viii) As $\beta \longrightarrow \infty$ (Newtonian case), the coefficient of skin friction, temperature profile, thermal, and momentum boundary layer thicknesses reduce, whereas the velocity and rate of heat transfer escalates

(ix) Increment of Cu-H_2O nanoparticle volume fraction into the Casson fluid boosts the heat transfer enhancement rate higher for the shrinking sheet surface

This present study on nanofluid heat transfer enhancement is valid for Casson's nanofluid and did not incorporate the effects of other important factors such as nanoparticle shape factors, hybrid nanoparticles, thermophoresis, and Brownian motion. We envisage extending this study in future to include other non-Newtonian nanofluids (both single and two phase flow models) and the effects of all the omitted factors.

Nomenclature

a, b: Real constants (s^{-1})
Bi: Biot number (convective parameter)
C_f: Coefficient of the skin friction
C_p: Specific heat at constant pressure of the fluid ($J\text{kg}^{-1}K^{-1}$)
Da: Darcy number (porous media parameter)
e_{ij}: The rate of strain tensor (s^{-1})
Ec: Eckert number
f: Dimensionless stream function
F: Forchheimer drag force coefficient (m^{-1})
F_r: Forchheimer (second order porous resistance) parameter
h_f: Convective heat transfer coefficient ($Wm^{-2}K^{-1}$)
k_1: Permeability of the porous medium (m^2)
k_f: Thermal conductivity of the base fluid ($W\ m^{-1}K^{-1}$)
k_s: Nanoparticles' thermal conductivity ($W\ m^{-1}K^{-1}$)
k_{nf}: Nanofluids' effective thermal conductivity ($W\ m^{-1}K^{-1}$)
L: Slip length coefficient ($\text{kgm}^{-1}s^{-2}$)
Nu_x: The local Nusselt number
Pr: Prandtl number
p_y: Yield stress of the fluid (Nm^{-2})
q_w: Heat flux (Wm^{-2})
S: Suction/injection (mass flux) Parameter
T: Temperature of the fluid (K)
T_f: Local fluid temperature (K)
T_∞: Ambient temperature of the Casson nanofluid (K)
u, v: Velocity components along x, y coordinates, respectively (ms^{-1})
U_∞: Free stream velocity of the Casson fluid (ms^{-1})
x, y: Coordinate along the plate and the transversal, respectively (m).

Greek Symbols

β: The non-Newtonian/Casson parameter/factor
δ: Velocity slip parameter
ε: Eigenvalue parameter
η: Similarity variable
θ: Dimensionless temperature
λ: Velocity ratio (stretching/shrinking) parameter
μ_B: Plastic dynamic viscosity of the Casson nanofluid ($Nm^{-2}s$)
μ_f: Dynamic viscocity of the base fluid ($\text{kgm}^{-1}s^{-2}$)
μ_{nf}: Effective dynamic viscosity of the Casson nanofluid (kgms^{-2})
ν_f: Kinematic viscocity of the base fluid (m^2s^{-1})
π: The $(i, j)^{\text{th}}$ component of deformation rate (Nm^{-2})
π_c: Critical value of π (Nm^{-2})
ρ_f: Density of the base fluid (kgm^{-3})
ρ_s: Density of the solid nanoparticle (kgm^{-2})
ρ_{nf}: Effective density of the Casson nanofluid (kgm^{-2})
$(\rho C_p)_{nf}$: Effective heat capacity of the Casson Nanofluid ($Jm^{-3}K^{-1}$)
τ: Nondimensional time variable
τ_{ij}: Components of stress tensor (Nm^{-2})
τ_w: Wall skin friction (Nm^{-2})
ϕ: Nanoparticle volume fraction.

Data Availability

Obtained numerical data were used to support the study.

Conflicts of Interest

We, the authors, declare no conflict of interest.

Acknowledgments

The authors gratefully acknowledge the financial support received.

References

[1] K. Bhattacharyya, "Boundary layer stagnation-point flow of Casson fluid and heat transfer towards a shrinking/stretching sheet," *Frontiers in Heat and Mass Transfer (FHMT)*, vol. 4, no. 2, 2013.

[2] N. Casson, "Flow equation for pigment oil suspensions of the printing ink type," *Rheology of Disperse Systems*, vol. 1, pp. 84–102, 1959.

[3] R. Saravana, M. Sailaja, and R. Hemadri Reddy, "Effect of aligned magnetic field on Casson fluid flow over a stretched surface of non-uniform thickness," *Engineering*, vol. 8, no. 1, pp. 283–292, 2019.

[4] X. Zhang, D. Yang, M. I. U. Rehman, and A. Hamid, "Heat transport phenomena for the Darcy–Forchheimer flow of Casson fluid over stretching sheets with electro-osmosis forces and Newtonian heating," *Mathematics*, vol. 9, no. 19, p. 2525, 2021.

[5] H. Upreti, A. K. Pandey, N. Joshi, and O. D. Makinde, "Thermodynamics and heat transfer analysis of magnetized casson hybrid nanofluid flow via a Riga plate with thermal radiation," *Journal of Computational Biophysics and Chemistry*, vol. 22, pp. 321–334, 2023.

[6] R. K. Tiwari and M. K. Das, "Heat transfer augmentation in a two-sided lid-driven differentially heated square cavity utilizing nanofluids," *International Journal of heat and Mass transfer*, vol. 50, no. 9-10, pp. 2002–2018, 2007.

[7] M. Gupta, V. Singh, and P. Katyal, "Synthesis and structural characterization of Al_2O_3 nanofluids," *Materials Today: Proceedings*, vol. 5, no. 14, pp. 27989–27997, 2018.

[8] S. U. S. Choi and J. A. Eastman, "Enhancing thermal conductivity of fluids with nanoparticles," Technical report, Argonne National Lab, Argonne, IL (United States), 1995.

[9] S. Özerinç, S. Kakaç, and A. G. Yazıcıoğlu, "Enhanced thermal conductivity of nanofluids: a state-of-the-art review," *Microfluidics and Nanofluidics*, vol. 8, 2010.

[10] M. Sheikholeslami, A. Zareei, M. Jafaryar et al., "Heat transfer simulation during charging of nanoparticle enhanced PCM within a channel," *Physica A: Statistical Mechanics and its Applications*, vol. 525, pp. 557–565, 2019.

[11] J. A. Eastman, S. U. S. Choi, W. Y. Sheng Li, and L. J. Thompson, "Anomalously increased effective thermal conductivities of ethylene glycol-based nanofluids containing copper nanoparticles," *Applied Physics Letters*, vol. 78, no. 6, pp. 718–720, 2001.

[12] M. Zubair, Z. Shah, A. Dawar, S. Islam, P. Kumam, and A. Khan, "Entropy generation optimization in squeezing magnetohydrodynamics flow of casson nanofluid with viscous dissipation and joule heating effect," *Entropy*, vol. 21, no. 8, p. 747, 2019.

[13] A. Saeed, Z. Shah, S. Islam et al., "Three-dimensional Casson nanofluid thin film flow over an inclined rotating disk with the impact of heat generation/consumption and thermal radiation," *Coatings*, vol. 9, no. 4, p. 248, 2019.

[14] S. A. Khan, M. I. Khan, T. Hayat, M. F. Javed, and A. Alsaedi, "Mixed convective non-linear radiative flow with TiO_2-Cu-water hybrid nanomaterials and induced magnetic field," *International Journal of Numerical Methods for Heat & Fluid Flow*, vol. 29, no. 8, pp. 2754–2774, 2019.

[15] R. Rizwana and S. Nadeem, "Series solution of unsteady MHD oblique stagnation point flow of copper-water nanofluid flow towards Riga plate," *Heliyon*, vol. 6, no. 10, article e04689, 2020.

[16] L. A. Lund, Z. Omar, S. Dero, I. Khan, D. Baleanu, and K. S. Nisar, "Magnetized flow of Cu + Al_2O_3 + H_2O hybrid nanofluid in porous medium: analysis of duality and stability," *Symmetry*, vol. 12, no. 9, p. 1513, 2020.

[17] A. Hussanan, M. Qasim, and Z.-M. Chen, "Heat transfer enhancement in sodium alginate based magnetic and non-magnetic nanoparticles mixture hybrid nanofluid," *Physica A: Statistical Mechanics and its Applications*, vol. 550, article 123957, 2020.

[18] T. Hayat, M. Sajid, and I. Pop, "Three-dimensional flow over a stretching surface in a viscoelastic fluid," *Nonlinear Analysis: Real World Applications*, vol. 9, no. 4, pp. 1811–1822, 2008.

[19] L. J. Crane, "Flow past a stretching *plate*," *Zeitschrift für Angewandte Mathematik und Physik*, vol. 21, no. 4, pp. 645–647, 1970.

[20] M. Tamoor, M. Waqas, M. Ijaz Khan, A. Alsaedi, and T. Hayat, "Magnetohydrodynamic flow of Casson fluid over a stretching cylinder," *Results in Physics*, vol. 7, pp. 498–502, 2017.

[21] C. Y. Wang, "Liquid film on an unsteady stretching surface," *Quarterly of Applied Mathematics*, vol. 48, no. 4, pp. 601–610, 1990.

[22] M. Miklavčič and C. Wang, "Viscous flow due to a shrinking sheet," *Quarterly of Applied Mathematics*, vol. 64, no. 2, pp. 283–290, 2006.

[23] C. Y. Wang, "Stagnation flow towards a shrinking sheet," *International Journal of Non-Linear Mechanics*, vol. 43, no. 5, pp. 377–382, 2008.

[24] R. Nazar, M. Jaradat, N. Arifin, and I. Pop, "Stagnation-point flow past a shrinking sheet in a nanofluid," *Open Physics*, vol. 9, no. 5, pp. 1195–1202, 2011.

[25] G. C. Layek, B. Mandal, K. Bhattacharyya, and A. Banerjee, "Lie symmetry analysis of boundary layer stagnation-point flow and heat transfer of non-newtonian power-law fluids over a nonlinearly shrinking/stretching sheet with thermal radiation," *International Journal of Nonlinear Sciences and Numerical Simulation*, vol. 19, no. 3-4, pp. 415–426, 2018.

[26] B. Mandal and G. C. Layek, "Unsteady MHD mixed convective Casson fluid flow over a flat surface in the presence of slip," *International Journal of Modern Physics C*, vol. 32, no. 3, article 2150038, 2021.

[27] S. A. Jumana, M. G. Murtaza, M. Ferdows, O. D. Makinde, and K. Zaimi, "Dual solutions analysis of melting phenomenon with mixed convection in a nanofluid flow and heat transfer past a permeable stretching/shrinking sheet," *Journal of Nanofluids*, vol. 9, no. 4, pp. 313–320, 2020.

[28] K. S. Tshivhi and O. D. Makinde, "Magneto-nanofluid coolants past heated shrinking/stretching surfaces: dual solutions and stability analysis," *Results in Engineering*, vol. 10, article 100229, 2021.

[29] N. S. Khashi'ie, N. M. Arifin, R. Nazar, E. H. Hafidzuddin, N. Wahi, and I. Pop, "Magnetohydrodynamics (MHD) axisymmetric flow and heat transfer of a hybrid nanofluid past a radially permeable stretching/shrinking sheet with Joule heating," *Chinese Journal of Physics*, vol. 64, pp. 251–263, 2020.

[30] F. B. Tadesse, O. D. Makinde, and L. G. Enyadene, "Mixed convection of a radiating magnetic nanofluid past a heated permeable stretching/shrinking sheet in a porous medium," *Mathematical Problems in Engineering*, vol. 2021, Article ID 6696748, 21 pages, 2021.

[31] P. Forchheimer, "Wasserbewegung durch boden," *Zeitschrift des Vereines Deutscher Ingenieure*, vol. 45, pp. 1782–1788, 1901.

[32] S. D. Harris, D. B. Ingham, and I. Pop, "Mixed convection boundary-layer flow near the stagnation point on a vertical surface in a porous medium: Brinkman model with slip," *Transport in Porous Media*, vol. 77, no. 2, pp. 267–285, 2009.

[33] A. S. Dogonchi, M. A. Sheremet, D. D. Ganji, and I. J. J. O. T. A. Pop, "Free convection of copper–water nanofluid in a porous gap between hot rectangular cylinder and cold circular cylinder under the effect of inclined magnetic field," *Journal of Thermal Analysis and Calorimetry*, vol. 135, no. 2, pp. 1171–1184, 2019.

[34] A. S. Sachin Shaw, M. K. N. Dogonchi, and O. D. Makinde, "Impact of entropy generation and nonlinear thermal radiation on Darcy-Forchheimer flow of MnFe2O4-Casson/water nanofluid due to a rotating disk: application to brain dynamics," *Arabian Journal for Science and Engineering*, vol. 45, no. 7, pp. 5471–5490, 2020.

[35] H. Upreti, A. K. Pandey, M. Kumar, and O. D. Makinde, "Darcy–Forchheimer flow of CNTs-H_2O nanofluid over a porous stretchable surface with xue model," *International Journal of Modern Physics B*, vol. 37, no. 2, article 2350018, 2023.

[36] N. Joshi, H. Upreti, and A. K. Pandey, "MHD Darcy-Forchheimer Cu-Ag/H_2O-$C_2H_6O_2$ hybrid nanofluid flow via a porous stretching sheet with suction/blowing and viscous dissipation," *International Journal for Computational Methods in Engineering Science and Mechanics*, vol. 23, no. 6, pp. 527–535, 2022.

[37] F. B. Tadesse, O. D. Makinde, and L. G. Enyadene, "Hydromagnetic stagnation point flow of a magnetite ferrofluid past a convectively heated permeable stretching/shrinking sheet in a Darcy–Forchheimer porous medium," *Sādhanā*, vol. 46, no. 3, pp. 1–17, 2021.

[38] M. Nakamura and T. Sawada, "Numerical study on the flow of a non-Newtonian fluid through an axisymmetric stenosis," *Journal of Biomechanical Engineering*, vol. 110, no. 2, pp. 137–143, 1988.

[39] I. L. Animasaun, "Effects of thermophoresis, variable viscosity and thermal conductivity on free convective heat and mass transfer of non-darcian MHD dissipative Casson fluid flow with suction and nth order of chemical reaction," *Journal of the Nigerian Mathematical Society*, vol. 34, no. 1, pp. 11–31, 2015.

[40] R. L. Hamilton and O. K. Crosser, "Thermal conductivity of heterogeneous two-component systems," *Industrial & Engineering Chemistry Fundamentals*, vol. 1, no. 3, pp. 187–191, 1962.

[41] S. W. Joseph, R. R. Colwell, and J. B. Kaper, "Vibrio parahaemolyticus and related halophilic vibrios," *CRC Critical Reviews in Microbiology*, vol. 10, no. 1, pp. 77–124, 1982.

[42] J. H. Merkin, "On dual solutions occurring in mixed convection in a porous medium," *Journal of Engineering Mathematics*, vol. 20, no. 2, pp. 171–179, 1986.

[43] P. D. Weidman, D. G. Kubitschek, and A. M. J. Davis, "The effect of transpiration on self-similar boundary layer flow over moving surfaces," *International Journal of Engineering Science*, vol. 44, no. 11-12, pp. 730–737, 2006.